Digital Beamforming Array Phase Calibration Techniques for Multi-Pass Interferometric SAR

A thesis submitted in partial fulfillment
of the requirements for the degree of
Master of Science in Electrical Engineering

by

KELLY CHEUNG
B.S.E.C.E., University of Rochester, 2019

2023
Wright State University

Wright State University
College of Graduate Programs & Honors Studies

November 28, 2023

I HEREBY RECOMMEND THAT THE THESIS PREPARED UNDER MY SUPERVISION BY Kelly Cheung ENTITLED Digital Beamforming Array Phase Calibration Techniques for Multi-Pass Interferometric SAR BE ACCEPTED IN PARTIAL FULFILLMENT OF THE REQUIREMENTS FOR THE DEGREE OF Master of Science in Electrical Engineering.

Brian D. Rigling, Ph.D.
Thesis Director

Michael A. Saville, Ph.D., P.E.
Chair, Department of Electrical Engineering

Committee on
Final Examination

Dr. Brian D. Rigling

Dr. Michael A. Saville

Dr. Fred Garber

Dr. Josh Ash

Shu Schiller, Ph.D.
Interim Dean,
College of Graduate Programs &
Honors Studies

ABSTRACT

Cheung, Kelly. M.S.E.E., Department of Electrical Engineering, Wright State University, 2023.
Digital Beamforming Array Phase Calibration Techniques for Multi-Pass Interferometric SAR.

Calibration plays a critical role in the optimal performance of algorithms in digital beamforming arrays. Phase incoherency between elements results in poor beamforming with decreased gain and higher sidelobes, leading to a decrease in accuracy and sensitivity of measurements. A similar problem exists in performing multi-pass interferometric SAR (IFSAR) processing of SAR data stacks to generate topological maps of the scene, where phase errors translate to height errors. By treating each SAR image in the data stack like an element of a uniform linear array, this thesis explores several phase calibration techniques that can be used to calibrate digital beamforming arrays and introduces them to IFSAR processing to calibrate the SAR images. Three data-driven techniques are selected, where calibration coefficients are obtain using sources of opportunity, via a contrast-based method, and via a clutter-based method. These calibration algorithms are then demonstrated on synthetic data of a simulated scene, consisting of scatterers at different heights, and with added phase incoherency to the SAR images. Processing of the simulated data shows an improvement in height estimation of the scatterers, including an evident increase in the gain and focusing of the scatterers in the scene after calibration. Phase calibration is then introduced to the processing of measured Gotcha data, where results also show gain and focusing improvement of the scatterers. Additional research, however, will be needed to associate the height estimation of the scatterers in these results with ground truth data to ascertain an absolute height map of the scene.

Contents

List of Figures

List of Tables

List of Symbols

Chapter 1

N	Total number of array elements
n	Element number
f_n	Input signal at the n^{th} element
τ_n	Time delay for the n^{th} element
g	Summation of delayed versions of f_n
(x, y, z)	Local East, North, Up Cartesian coordinates

Chapter 2

D_{ff}	Far field distance
λ	Wavelength
D	Longest dimension of the antenna
N	Total number of array elements
d	Element spacing
θ	Angle of arrival
τ	Time delay between adjacent elements
c	Speed of light
ϕ	Phase difference between adjacent elements
λ	Wavelength
$E_a(\theta)$	Beam pattern
$E_e(\theta)$	Elements' radiation pattern
$AF(\theta)$	Array factor
G_a	Array gain
θ_b	3-dB beamwidth
n	Sensor element index
S_n	n^{th} sensor
(x, y, z)	Local East, North, Up Cartesian coordinates
$I_n(x, y)$	n^{th} SAR image from S_n for pixel locations (x, y)
B	Baseline
φ	Look angle
α	Interferometer tilt angle
h, H	Height
P	Point on terrain
R	Slant range from sensor to point P
ΔR	Difference in slant range between two sensors
t	Time
l	Transmitted signal
m	Received signal
A	Amplitude
f_c	Center frequency

Θ	Signal phase offset
Φ	Interferometric phase
Φ_F	Flat Earth phase difference
Φ'	Interferometric phase with flat Earth phase difference correction
P_F	Reference point on flat terrain
R_F	Slant range from sensor to point P_F
ΔR_F	Difference in slant range from two sensors to point P_F
B_c	Critical baseline
$B_{c\perp}$	Perpendicular component of the critical baseline
$(\omega_x, \omega_y, \omega_z)$	Local East, North, Up Cartesian coordinates in the image-Fourier domain
Δz	Height resolution
v	Time domain signal
V	Fourier domain signal
$\Delta\omega_z$	ω_z resolution
z_{un}	Unambiguous height

Chapter 3

(x, y, z)	Local East, North, Up Cartesian coordinates
(x_1, y_1, z_1)	(x, y, z) coordinates for simulated scatterer 1
(x_2, y_2, z_2)	(x, y, z) coordinates for simulated scatterer 2
(x_3, y_3, z_3)	(x, y, z) coordinates for simulated scatterer 3
σ^2	Additive white Gaussian noise variance
n	Sensor element index
E	Entropy
$\vec{I}$	Stack of SAR images
$\vec{I_{fft}}$	Fourier transform of $\vec{I}$
$\vec{p}$	Normalized energy
ν	Voxel index
N_ν	Total number of voxels
d	Element spacing
λ	Wavelength
$\vec{\theta}$	Angle of arrival of all the calibration sources
N	Total number of array elements
M	Number of calibration sources
$\vec{T}$	Stack of cropped $\vec{I}$
Υ	Total number of x or range bins in $\vec{T}$
N_y	Total number of y or cross range bins in $\vec{T}$
$\vec{c}$	Phase calibration coefficients
$\vec{\zeta}$	Residual phase error, with linear and average components removed

Chapter 4

(x, y, z)	Local East, North, Up Cartesian coordinates

Acknowledgment

I would like to first thank my advisor, Dr. Brian Rigling, for his expertise and guidance during the research and development of this thesis, including image formation scripts, code debugging, and the many technical discussions on signal processing and IFSAR. I would also like to thank Dr. Michael Saville, Dr. Fred Garber, and Dr. Josh Ash for serving on my thesis commitee. I also thank Dr. Paul Sotirelis for helping me understand SAR principles. Finally, I would like to express my appreciation for the encouragement and support of my colleagues at the Air Force Research Laboratory.

Dedicated to

AFRL/RYDR

Chapter 1

Introduction

In order to obtain accurate measurements, sensor systems must be first calibrated to a known state through performing a calibration routine. The calibration routine compensates for unknown errors that degrade the performance of the system. These errors may stem from manufacturing, environmental effects, and other hardware changes. The robustness of the calibration procedure has implications on how well algorithms perform, which can affect the sensitivity and resolution of a sensor system.

1.1 Motivation

The calibration problem is prevalent in many areas of sensor research. For example, calibration techniques play a critical role in aligning the amplitudes and phases between elements for phased arrays in radar systems. Phased arrays consist of a collection of antenna elements with electronic hardware such as phase shifters or time delay units. Each antenna element has its own radiation pattern. The combination of these radiation patterns forms a beam; a classical example is the delay-and-sum beamformer. The delay-and-sum beamformer is shown in Figure 1.1, where a plane wave is impinging on the N-element array; f_n denotes the input signal for the n^{th} element, τ_n denotes the time delay for the n^{th} element, and g represents the summed signal. When a transmit/receive (T/R) module [1] is placed behind each element and beamforming is enabled by varying the complex weights electronically to control the beam shape and steering angle, this is known as an active electronically scanned array (AESA). By beamforming, AESAs optimize the sensitivity and directivity of the radar.

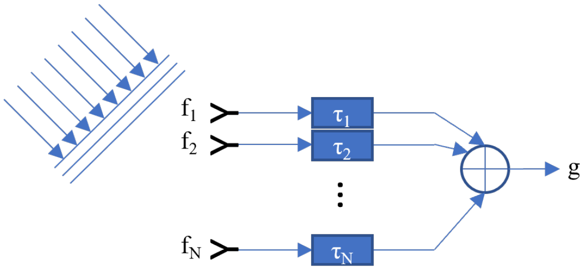

Figure 1.1: Delay-and-sum beamformer

Additional flexibility in beamforming applications can be achieved with a digital back-end and element-level digitization, enabling digital beamforming (DBF). Some benefits of elemental DBF are discussed in [2], which include the creation of multiple, simultaneous, independently steerable receive beams, improvements in dynamic range, and reconfigurability. A high level example architecture is shown in Figure 1.2, consisting of the radio frequency (RF) front-end, data converters, and digital beamformer. Examples of digital phased arrays featuring element-level DBF include the Space Fence [3], Horus [4], and FlexDAR [5].

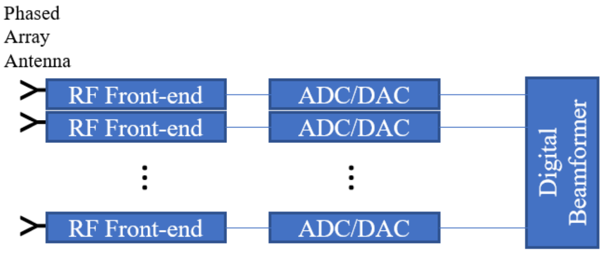

Figure 1.2: Example of a digital phased array architecture

For a digital phased array, the amplitude and phase imbalance between elements that necessitate calibration can come from a variety of sources. The path loss will likely differ from element to element due to the manufacturing tolerance of components, electrical interconnects, and cabling as well as the frequency of operation. The ADCs or DACs may not be phase locked or have residual phase errors from poor sample clock synchronization. Furthermore, environmental factors such as temperature changes and system vibrations may also introduce errors and require recalibration of the system in the field.

Many calibration approaches have been developed to tackle the phased array calibration problem. Several of these approaches are mentioned in [2], which include the use of a far field antenna, near-field probing, internal calibration networks, mutual coupling, and clutter returns. Other calibration approaches include calibration using targets with a high signal to noise (SNR) ratio [6] and optimization based on contrast metrics [7].

Similar calibration problems exist for multi-channel, multi-baseline, and multi-pass synthetic aperture radar (SAR) applications. With multi-channel SAR, DBF architectures enable new modes for achieving high resolution and wide swath SAR imaging as discussed in [8]. It is expected that this requires calibration between each digital channel for optimal imaging performance, and works such as [9] have modelled the effects of errors with respect to the sensitivity and range ambiguity metrics for such a system. Similar calibration approaches have been explored by [10] and [11] with the inclusion of an internal calibration network and data-driven approaches for the calibration of a multi-channel spaceborne SAR system. The data-driven calibration approaches include the previously mentioned use of radar clutter returns and contrast-based metrics. The authors of [12] further improve on the approach of leveraging the spatial correlation between channels from clutter returns of [13] by taking into account angular variations in elevation to minimize residual calibration errors.

Similarly, for multi-baseline or multi-pass/repeat-pass configurations that may be used for interferometric SAR (IFSAR) and 3D SAR tomography (TomoSAR), phase calibration between SAR data collected at different sensor locations should be performed. This is to mitigate phase incoherencies across the data stack that may come from sensor location uncertainty and atmospheric propagation delays, in addition to the channel imbalances that exist for the multi-channel case. For multi-pass IFSAR, the phase difference observed from at least two different look angles can be used to resolve a topological map of the scene. As a result, any phase inconsistencies between data collected at different sensor locations during successive passes directly translate to height uncertainty in the resulting digital elevation model (DEM). Leveraging multiple baselines, multiple interferograms for IFSAR have been explored to decrease errors in height estimation as shown by [14] and [15]. Furthermore, multiple baselines with flight trajectories of varying heights enable tomographic processing to obtain a distribution of the height response from objects in the scene based on differences in scattering properties observed in elevation [16]. However, phase variations cause defocusing of the tomograms as analyzed in [17]. Therefore, methods to phase calibrate the SAR data stacks for both IFSAR and TomoSAR have been proposed in many works including [18] and [19].

As sensor systems become more complex, the task of calibration becomes more challenging, making the calibration problem an active research area. Solutions to the problem are relevant to a variety of applications that involve sensor array processing to maximize algorithmic performance. Different calibration approaches have different hardware and environment requirements. The choice of which calibration approach(es) to implement ultimately depends on its suitability to the application and is made with consideration of the trade-offs in hardware and computational complexity.

1.2 Research Goal and Approach

The goal of this research is to leverage different calibration algorithms that can be used to calibrate digital beamforming arrays and apply them to SAR data stacks consisting of data collected during successive passes in a multi-pass IFSAR configuration. The data stacks contain data from multiple look angles at different elevations, which can be interferometrically processed to form a height map of the scene. By treating data collected at different look angles like data collected at each element of a digital array, similar calibration techniques can be applied to the data stack. For simplicity, a linear array configuration and phase calibration is considered in this work. Height maps are generated from the uncalibrated and calibrated data stacks, which are then compared against ground truth data to determine the performance improvement in height estimation after phase calibration.

To begin, a literature search is performed to obtain a selection of applicable array calibration algorithms. Since this research leverages previously collected SAR data, data-driven calibration approaches are the most applicable. Three phase calibration algorithms are selected to be implemented and demonstrated in MATLAB for simulated and measured data. The first algorithm is from [6], which relies on known calibration sources to compute the phase difference between elements given the linear array geometry. The second algorithm is shown in [7] and [18], where phase calibration is achieved when the expected value of the contrast of the beamformed data is maximized. Lastly, the third algorithm is from [13], which uses the statistical properties of homogeneous data to correlate the element data to obtain the phase differences.

Analogous to an 8-element linear array with amplitude and phase errors, SAR images for 8 different passes at different elevation angles are simulated for a scene containing 3 point scatterers at different heights. Phase errors and noise are added to the images. These images are beamformed to obtain a relative height map of the scene and demonstrate the effect of the phase incoherencies and noise on the resulting height estimation. Then, IFSAR processing is repeated to generate height maps after each of the phase calibration algorithms are applied to the images. Results are compared with the simulated height of the scatterers in the scene.

The algorithms are similarly applied to calibrate a stack of SAR images formed from the Gotcha Volumetric SAR dataset [20]. The SAR data was collected at X-band (9.6 GHz) with a 640 MHz bandwidth and full polarization. In this work, data from the horizontal transmit and horizontal receive, ‘HH’, polarization is used. The SAR images are formed using the backprojection algorithm for 3 degrees in azimuth. This data set contains 8 passes in its flight path, with each pass at a different elevation, as shown in Figure 1.3. By selecting points along the flight trajectory, synthetic apertures across the different passes can be formed. Then, the data collected at each point can be treated analogously to the RF data from each element of a digital phased array and subsequently calibrated. Two example array configurations, “Array 1” and “Array 2”, are shown in Figure 1.3, where the array elements represent the points in azimuth at which the SAR data was collected. Data from the first 8 passes in the “Array 2” configuration will be used to demonstrate the phased array calibration algorithms in this work.

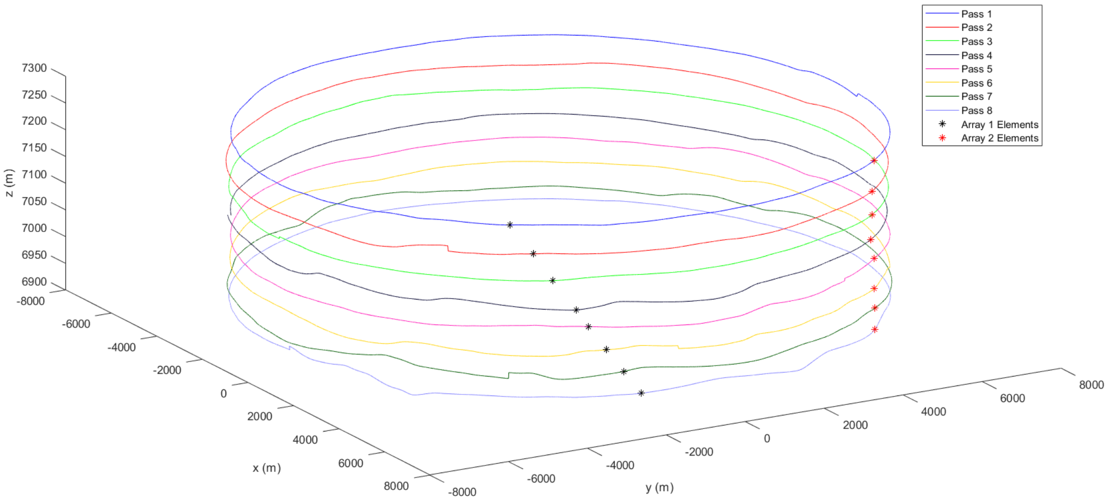

Figure 1.3: Data flight trajectory

1.3 Thesis Outline

The remainder of this thesis is divided into four chapters: background and theory, algorithms, analysis and results, and conclusion. The background and theory chapter provides the mathematical foundation for phased arrays, digital beamforming, and IFSAR processing. The algorithms chapter presents the implementation of the data-driven calibration algorithms. The analysis and results chapter presents the results of IFSAR processing, including the relative height maps for uncalibrated and calibrated simulated and measured data. The relative height maps are compared with ground truth data of the known altitude of several scatterers in the scene. Finally, the conclusion summarizes the impact of this research and future work.

Chapter 2

Background and Theory

This chapter summarizes the key fundamental principles and mathematical concepts for array and interferometric SAR processing required in the development of this work. First, phased array antenna theory and DBF are discussed. With this background, the effects of amplitude and phase errors on an antenna's radiation pattern are demonstrated. Next, IFSAR processing to generate an interferogram and the computation of a topological map with SAR data from two look angles are discussed. Here, it is shown that height error is proportional to phase error. IFSAR processing is then extended to include data from multiple look angles at different elevations that are beamformed to create the composite height map.

2.1 Digital Phased Arrays

Like for traditional analog phased arrays, a defining factor in the performance of a digital phased array are its elements. A simple case is the uniform linear array (ULA), as shown in Figure 2.1. When the antenna is receiving a signal from a source that is sufficiently far away, termed "far field," the signal approximates that of a plane wave at the array. Any curvature of the wavefront seen at the elements will introduce phase incoherencies between the elements. The approximation of the far field distance, D_{ff}, is typically given by

$$D_{ff} \geq \frac{2D^2}{\lambda} \tag{2.1}$$

where λ is the wavelength of the signal and D is the largest dimension of the radiating antenna. For the ULA, D is equivalent to $(N-1)d$, where N is the number of elements and d is the element spacing.

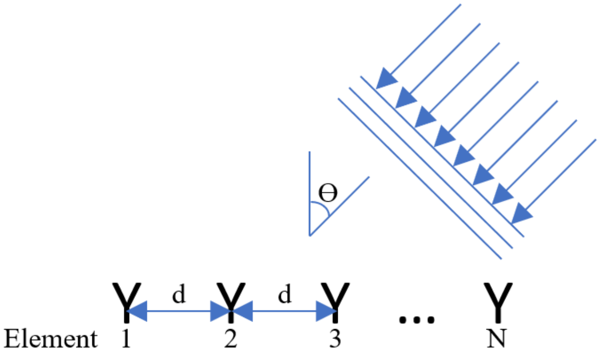

Figure 2.1: Uniform linear array

If a plane wave is impinging on the array at an angle θ as shown in Figure 2.1, the signal will be received by elements from right to left with an increasing delay. The time delay between adjacent elements, τ, is defined by

$$\tau = \frac{d \sin(\theta)}{c} \tag{2.2}$$

where d is the element spacing and c is the speed of light.

The equivalent computation in terms of the phase difference ϕ is given by

$$\phi = \frac{2\pi d \sin(\theta)}{\lambda} \tag{2.3}$$

where λ is the signal wavelength. Therefore, the steering angle of the beam in the direction of the plane wave can be achieved through the compensation of the time delays (for wideband arrays) or phase differences (for narrowband arrays) observed by the elements. This is further discussed in [21], where true time delay is demonstrated to offer significantly better performance over phase shifts for wide bandwidths.

Since the beam pattern is the array response from the coherent excitation of the elements, it can be synthesized by collecting element data of incident plane waves over the field of view. The combination of the elements' radiation patterns offers improvements in SNR over a single element by achieving array gain. The gain improvement is computed in decibels (dB) by

$$G_a = 20\log_{10}(N) \tag{2.4}$$

where N is the total number of elements. Mathematically, the beam pattern, $E_a(\theta)$, is given by

$$E_a(\theta) = E_e(\theta) \cdot AF(\theta) \tag{2.5}$$

where $E_e(\theta)$ is the elements' radiation pattern and $AF(\theta)$ is the array factor at angle θ radians. For a ULA, the array factor is given by

$$AF(\theta) = \frac{\sin\left(\frac{N\pi d\sin(\theta)}{\lambda}\right)}{N\sin\left(\frac{\pi d\sin(\theta)}{\lambda}\right)} \tag{2.6}$$

as also shown in [22], where N is the total number of elements, d is the element spacing, λ is the wavelength, and θ is the angle in radians. The author of [21] shows the substitution of (2.3) in computing (2.6) and expands it to include beam steering with time delays or phase shifts.

Key parameters of note for the beam pattern are the 3-dB beamwidth and sidelobe levels. The beamwidth determines the angular resolution and is the width measured between the points 3 dB below the peak of the main lobe. The 3-dB beamwidth, θ_b, is approximated in radians by

$$\theta_b \approx 2\sin^{-1}\left(0.446\frac{\lambda}{Nd}\right) \tag{2.7}$$

in [23] for a ULA with isotropic elements and broadside beam at 0°. It is clear that a larger array provides a finer sensing resolution. The author of [24] elaborates on (2.7) with an approximation showing that an increase in steering angle off broadside results in an increase in beamwidth. Additionally, low sidelobes are desired to maximize the array's sensitivity. To lower the sidelobe levels, amplitude tapering with functions such as those shown in [25] can be used; however, this typically comes with a trade-off resulting in a wider beamwidth and decreased antenna gain.

2.1.1 Digital Beamforming

A digital phased array substantially improves the flexibility of beamforming over a traditional analog phased array. In an element-level DBF architecture, the RF signal is digitized per element and processed in the digital domain. Multiple beams can be synthesized and steered towards the directions of interest, as shown in Figure 2.2 for a calibrated array. Importantly, given the digitized signal for each element, data-driven calibration approaches can be leveraged to determine the amplitude and phase incoherency between the elements.

2.1.2 Impact of Amplitude and Phase Errors on Beamforming

To demonstrate how array performance is impacted by amplitude and phase errors, a ULA with 8 isotropic elements and $\frac{\lambda}{2}$-element spacing is simulated in MATLAB. The center frequency is 9.6 GHz. When the array is calibrated, the beam pattern for a beam at 0° is

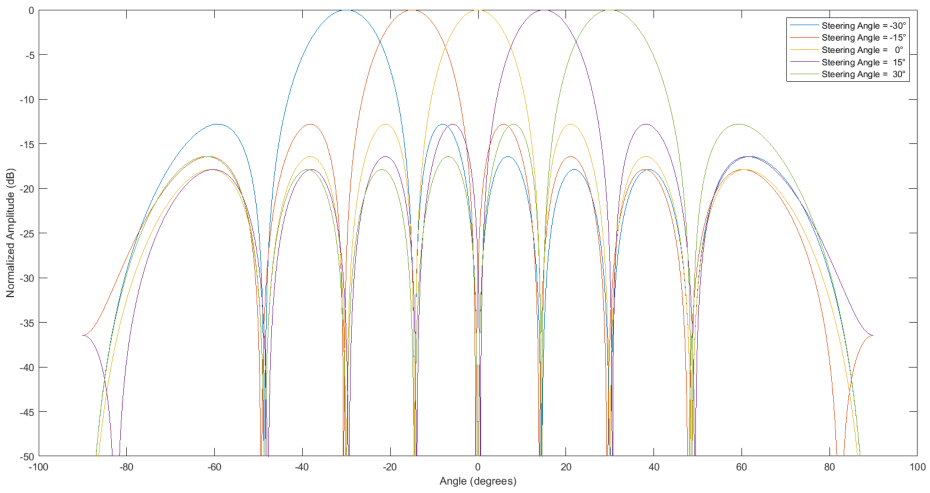

Figure 2.2: Beam patterns of a calibrated 8-element ULA

as shown in Figure 2.2. To simulate an uncalibrated array, Gaussian-distributed amplitude and phase errors are applied to each element. The amplitude errors have a mean of 0 dB and standard deviation of 3 dB. The phase errors have a mean of 0 radians and standard deviation of $\frac{\pi}{2}$ radians. Figure 2.3 shows that the performance of the array may suffer from high sidelobes, inaccurate steering angle, decreased gain, and poor spatial resolution. Further statistical analysis of these effects is summarized in Chapter 9 of [24].

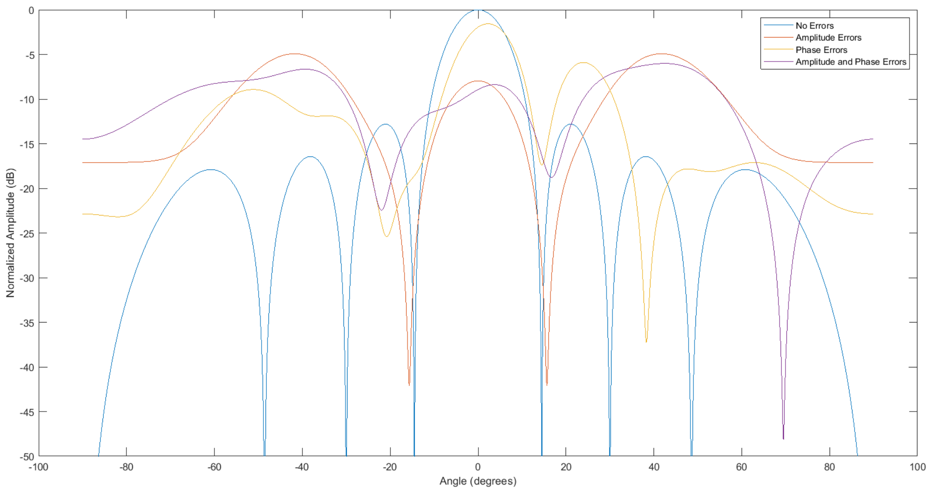

Figure 2.3: Beam patterns of an uncalibrated 8-element ULA

2.2 Interferometric SAR

One application of IFSAR is the generation of topological maps of a scene by collecting data from different look angles and converting the phase differences observed into height equivalents. This data can be collected under different sensing geometries, for example, with multiple sensors on an aircraft or satellite in a single-pass configuration or with one sensor at different points along its trajectory in a multi-pass configuration. The general IFSAR processing steps for the data used in this work are shown in Figure 2.4, modified from [26] [14], which include image formation, image registration, phase calibration, interferogram generation and beamforming, height map generation, and orthorectification. The focus of this work is with the addition of the phase calibration step. Other key processing steps used to support this work are briefly summarized in this section.

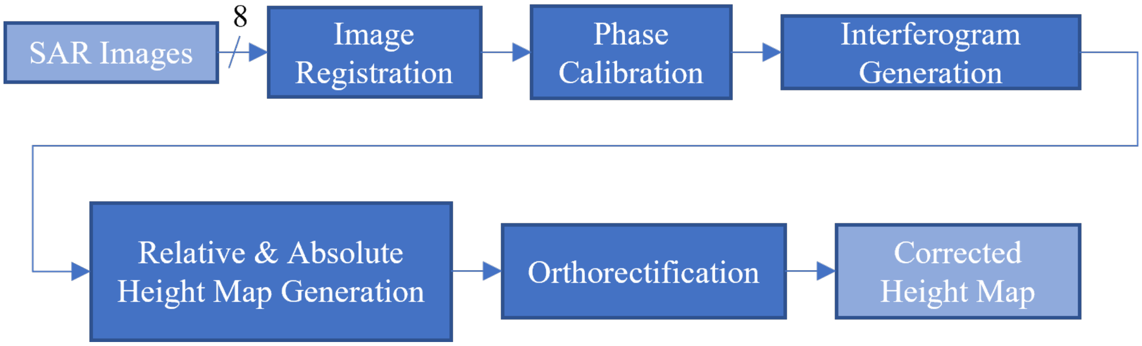

Figure 2.4: Modified IFSAR processing steps

The first step of processing is to form the SAR images from the SAR phase history data. This can be accomplished via the polar format algorithm [27] or backprojection algorithm [28]. Next, image registration is performed to spatially align the SAR images, $I_n(x, y)$ for n = 1, 2, ... N total images, such that the pixel at $I_n(x, y)$ for n = 2 ... N corresponds to the pixel from $I_1(x, y)$ of the scene. This step corrects for any translation or rotation of the scene between the images on the order of pixel to sub-pixel accuracy. Registration can be accomplished by control point mapping [26] or with intensity-based techniques as done in this work using the *imregtform* function in the Image Processing

Toolbox in Matlab [29]. The SAR images are resampled to ensure that the data is also uniform in the altitude dimension. Then, the interferograms for pairs of images can be formed. This can be equivalently accomplished by beamforming the set of SAR images, which results in a relative height map in the form of a 3D point cloud. An absolute height map can then be formed through peak finding across elevation and if given the known height of a scatterer in the scene. Lastly, the orthorectification step corrects for range and cross range pixel location errors due to foreshortening and/or layover effects. Foreshortening or layover effects exist due to differences in slant ranges measured from the sensor to the scatterers relative to that of those measured from the ground, resulting in scatterers to appear either closer or farther away.

2.2.1 IFSAR with Two Look Angles

To develop the mathematical basis for IFSAR processing, the simple sensing geometry with two look angles is considered. This is shown in Figure 2.5, where S_n is the location of the n^{th} sensor for n = 1, 2, ... N total sensors, B is the baseline between the two sensor locations, φ is the look angle, and α is the tilt angle of the interferometer relative to the x-y plane. In this case, x is the ground range and y is the cross range. S_1 is located at height $z = H$. A scatterer, P, at x with height $z = h$ is also shown. The phase difference observed between the two sensors, known as the interferometric phase, due to the difference in slant range, ΔR, can then be computed.

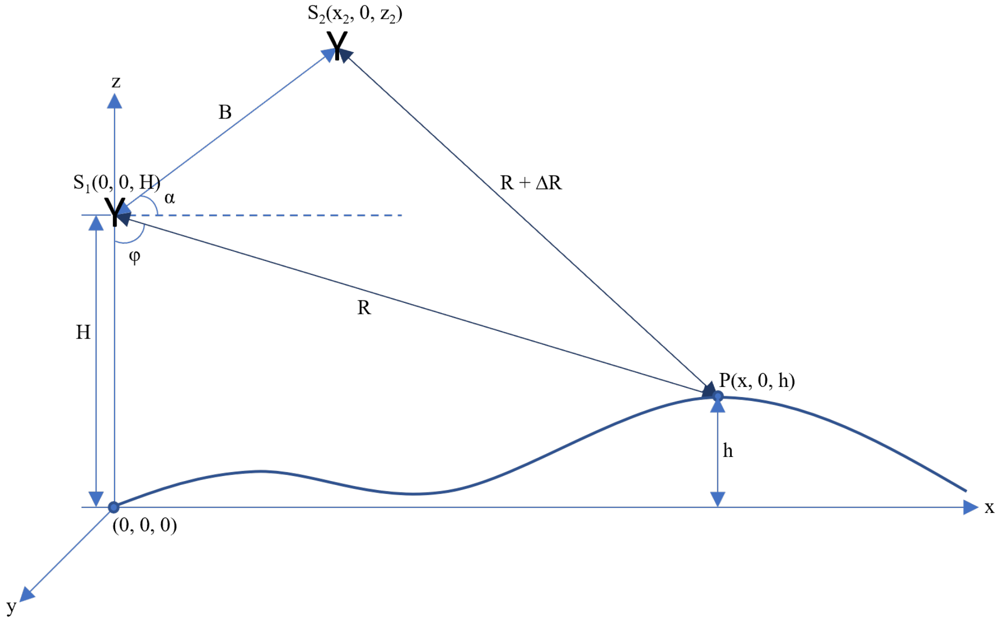

Figure 2.5: Geometry for IFSAR with 2 sensors

First, consider the transmitted signal, $l(t)$ for time t, as given by

$$l(t) = Ae^{-j(2\pi f_c t + \Theta)} \tag{2.8}$$

where A is the amplitude, f_c is the frequency, and Θ is the phase. The received signal at S_1 and S_2, $m_1(t)$ and $m_2(t)$ respectively, is the scaled and delayed version of $l(t)$ based on the two way slant range distance traveled that is depicted in Figure 2.5. $m_1(t)$ and $m_2(t)$ are given by

$$m_1(t) = A_1 e^{-j(2\pi f_c(t - \frac{2R}{c}) + \Theta)} = A_1 e^{-j(2\pi f_c t - \frac{4\pi R}{\lambda} + \Theta)} \tag{2.9}$$

and

$$m_2(t) = A_2 e^{-j(2\pi f_c(t - \frac{2(R+\Delta R)}{c}) + \Theta)} = A_2 e^{-j(2\pi f_c t - \frac{4\pi R}{\lambda} - \frac{4\pi \Delta R}{\lambda} + \Theta)} \tag{2.10}$$

where c is the speed of light and λ is the wavelength.

The interferometric phase, Φ, can be computed by multiplying m_1 with the complex conjugate of m_2 as shown by

$$\Phi = arg(m_1 \cdot \overline{m_2}) = \frac{4\pi\Delta R}{\lambda} \tag{2.11}$$

For all the pixels in the image, Φ is computed to generate an interferogram. However, the resulting interferometric phases require compensation of the phase difference observed from a flat scene Φ_F, also known as the flat Earth phase difference, as discussed in [26] and [30]. Φ_F is computed in (2.12) with the same geometry from Figure 2.5, but to a reference point on flat terrain, P_F, where ΔR_F denotes the difference in slant range from S_1 to P_F and S_2 to P_F. The corrected interferometric phase, Φ', is then computed by

$$\Phi_F = \frac{4\pi\Delta R_F}{\lambda} \tag{2.12}$$

and

$$\Phi' = \Phi - \Phi_F \tag{2.13}$$

By applying the law of cosines to the sensing geometry in Figure 2.5, ΔR can be computed[1] with

$$\begin{aligned}(R + \Delta R)^2 &= R^2 + B^2 - 2BR\sin(\varphi - \alpha) \\ \Delta R &= \sqrt{R^2 + B^2 - 2BR\sin(\varphi - \alpha)} - R \end{aligned} \tag{2.14}$$

Let the slant range from S_1 to P_F be R_F and from S_2 to P_F be R_F+ΔR_F. Then, following (2.14) and recasting it in terms of altitude of S_1, H, and x, as demonstrated in [26], R_F is computed according to

---

[1] $\Delta R \approx -B\sin(\varphi - \alpha)$ if R is assumed to be sufficiently large such that $R \gg B$ and $R \gg \Delta R$.

$$\begin{aligned}\Delta R_F &= \sqrt{R_F^2 + B^2 - 2BR_F\sin(\varphi(x) - \alpha)} - R_F \\ &= \sqrt{R_F^2 + B^2 - 2BR_F(\frac{x}{R_F}\cos(\alpha) - \frac{H}{R_F}\sin(\alpha))} - R_F \\ &= \sqrt{H^2 + x^2 + B^2 - 2B(x\cos(\alpha) - H\sin(\alpha))} - \sqrt{H^2 + x^2} \end{aligned} \tag{2.15}$$

where

$$R_F = \sqrt{H^2 + x^2} \tag{2.16}$$

To relate the interferometric phases to heights, the geometry in Figure 2.5 shows that the height of a scatterer, z, can be computed by

$$z = H - R\cos(\varphi) \tag{2.17}$$

By the law of cosines, the look angle φ is given by

$$\begin{aligned}(R + \Delta R)^2 &= R^2 + B^2 - 2BR\sin(\varphi - \alpha) \\ \varphi &= \alpha + \sin^{-1}\left(\frac{B}{2R} - \frac{\Delta R^2}{2BR} - \frac{\Delta R}{B}\right)\end{aligned} \tag{2.18}$$

By substitution of (2.11) and (2.18) into (2.17) as demonstrated in [31] and applying this to each pixel at locations (x, y), a relative height map can be formed by

$$\begin{aligned}z(x, y) &= H - R(x, y)\cos\big(\alpha + \sin^{-1}(\eta)\big) \\ &= H - R(x, y)(\sin(\alpha)\sqrt{1 - \eta^2} + \cos(\alpha)\eta)\end{aligned} \tag{2.19}$$

where

$$\eta = \frac{B}{2R(x, y)} - \frac{(\Phi'(x, y)\lambda)^2}{(4\pi)^2 2BR(x, y)} - \frac{\Phi'(x, y)\lambda}{4\pi B} \tag{2.20}$$

2.2.2 Effects of Phase Errors on IFSAR Height Estimation Accuracy

From (2.19), it is evident that errors in the measurements of the range, baseline, tilt angle, and interferometric phase impact the determined height of each pixel. As demonstrated in [26] and [31], a measure of the sensitivity of the height estimation due to such errors can be computed by taking the derivative of the height function with respect to each parameter. For example, any phase errors introduced to or originating from the sensor itself will cause errors in the interferometric phases Φ'. Therefore, the height sensitivity due to phase errors can be derived by taking the derivative of z with respect to Φ'. By combining the derivations of (2.12), (2.17), and (2.18), this computation is shown by

$$\begin{aligned}
\frac{\mathrm{d}z}{\mathrm{d}\Phi'} &= \frac{\mathrm{d}z}{\mathrm{d}\varphi} \cdot \frac{\mathrm{d}\varphi}{\mathrm{d}\Delta R} \cdot \frac{\mathrm{d}\Delta R}{\mathrm{d}\Phi'} \\
&= R\sin(\varphi) \cdot -\frac{R+\Delta R}{BR\cos(\varphi-\alpha)} \cdot \frac{\lambda}{4\pi} \\
&= -\frac{\lambda \sin(\varphi)(R+\Delta R)}{4\pi B\cos(\varphi-\alpha)} \\
\therefore dz &= -\frac{\lambda \sin(\varphi)(R+\Delta R)}{4\pi B\cos(\varphi-\alpha)} d\Phi' \qquad (2.21)
\end{aligned}$$

This demonstrates that the height is less sensitive to phase errors given a larger baseline and smaller wavelength. While a larger baseline decreases the height sensitity to phase errors, it is important to also note that there is a limit to the maximum baseline to prevent spatial baseline decorrelation of the signals of corresponding pixels between the two sets of SAR data. This baseline is known as the critical baseline, B_c, as discussed in [32] [33]. Only the perpendicular component of B_c, $B_{c\perp}$, is considered to contribute to decorrelation in [33]. This is provided by

$$B_{c\perp} = \left| \frac{RB\tan(\varphi-\alpha)}{f_c} \right| \qquad (2.22)$$

where λ is the wavelength, R is the slant range to the center of the resolution cell, φ is the look angle, B is the bandwidth, f_c is the frequency, and α is the interferometer tilt angle.

The maximum baseline before data are expected to decorrelate for the Gotcha dataset is estimated by $B_{c\perp} = \left|\frac{RB\tan(\varphi-\alpha)}{f_c}\right| = \left|\frac{(9997.98m)(640MHz)(tan(45.92°-90°))}{9.6GHz}\right| = 645.46$m, where R is the range to scene center and φ is the look angle for Pass 8. With the "Array 2" configuration (Figure 1.3), α is 90°. The maximum baseline is the altitude difference between Pass 1 and Pass 8, which is 314m. Since this is less than $B_{c\perp}$, data from the largest baseline used are not spatially decorrelated.

2.2.3 IFSAR with Multiple Look Angles

IFSAR for two look angles can be viewed as the simplest case of multiple look angles obtained from a multi-pass configuration. The authors of [34] discuss this with respect to 3-D SAR processing, demonstrating that an IFSAR product, the height map of the scene, can be similarly achieved by considering a set of collection planes, formed from different look angles, like a sparse array and processing them in the Fourier domain. Therefore, IFSAR processing for multiple look angles is reframed as a sampling problem, where the images, or looks from successive passes, are equivalently viewed as samples in elevation. Processing steps are shown in Figure 2.6. The image data are, first, moved to the image-Fourier domain, where ω_x, ω_y, and ω_z are the corresponding local East, North, Up Cartesian coordinates transform equivalents in this domain. For uniform spacing in all dimensions, the data are then resampled along ω_z. This is required because the collection planes from the successive passes are not necessarily uniform, as shown in Figure 2.7 for the Gotcha dataset. The discrete Fourier transform

$$V[k] = \sum_{n=0}^{N-1} v[n]e^{-\frac{j2\pi kn}{N}} \qquad k = 0, 1, ...N-1 \quad (2.23)$$

can then be applied to the vector of samples, $\vec{v}$, for each collocated pixel in the images of the scene to resolve the height of the scatterers. These separate transform operations are equivalent to performing a 3-D FFT. The resulting beamformed data are related to the corresponding elevations, $\vec{z}$, by

$$z[n] = \frac{cn}{2\pi N \Delta\omega_z} \qquad n = 0, 1, ...N-1 \quad (2.24)$$

to form the relative height map. The difference between two successive elevation samples gives the resolved height resolution, Δz. Absolute height map generation and orthorectification is then performed, as in Figure 2.4, to obtain the corrected height map.

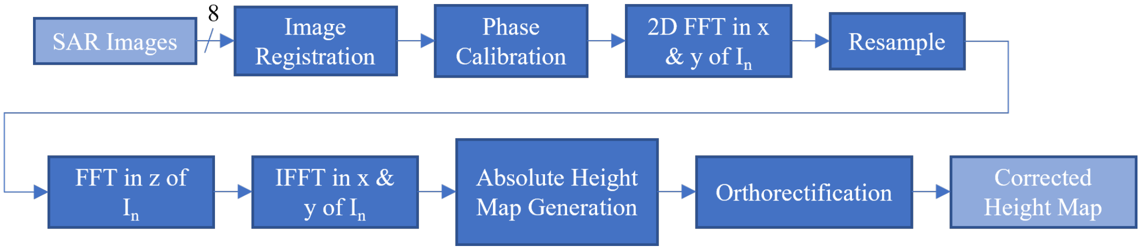

Figure 2.6: Processing steps for IFSAR with multiple look angles

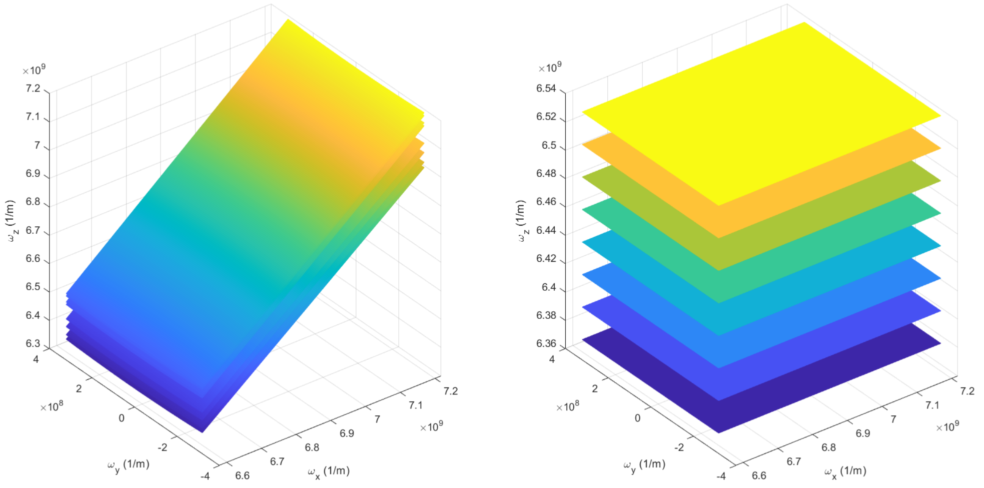

Figure 2.7: Collection planes of Gotcha data (original showing non-uniform ω_z, on the left, and with resampling for uniform ω_z, on the right)

2.2.4 Orthorectification

Orthorectification, or foreshortening and layover correction, is the process during which the ground range and cross range pixel location error is corrected for in the height map. These errors exist due to the differences in slant ranges from the sensor to the scatterers, resulting in the ambiguity of whether a radar return is from a scatterer at an elevated height or on the ground at the same range, as explained by [26]. Considering points on the same range plane as scatterer P at pixel location (x, y) in the geometry of Figure 2.8, the corrected ground range for each pixel, x_c, is related to the height h and the look angle φ by

$$x_c = x + h(x, y)\tan\left(\frac{\pi}{2} - \varphi\right) \tag{2.25}$$

The shift in ground range, Δx, is then given by

$$\Delta x = x_c - x \tag{2.26}$$

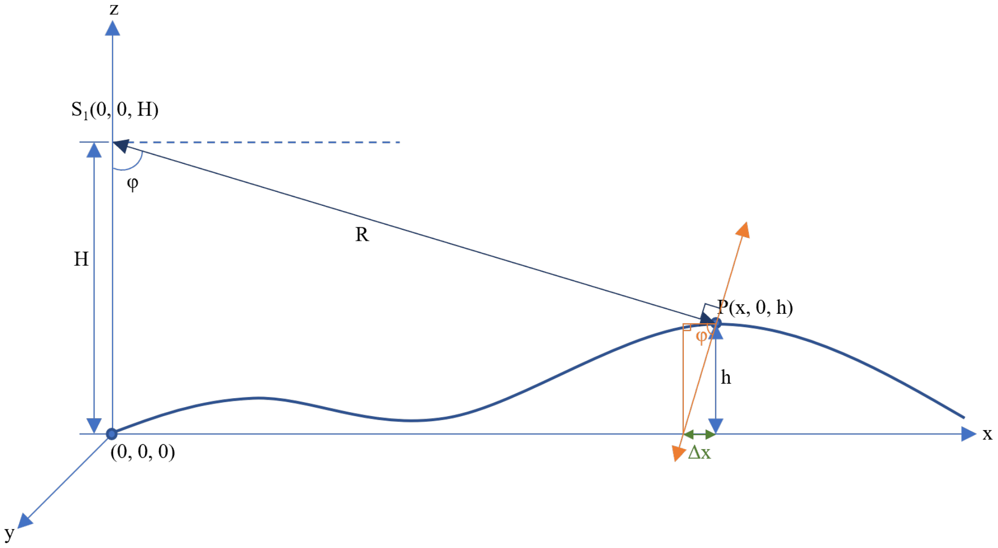

Figure 2.8: Orthorectification geometry to determine ground range, x, correction

2.2.5 Unambiguous Height

Due to undersampling of the vertical dimension, aliasing in the resolved height of the scatterers will occur. In this case, it is important to consider the unambiguous height resolution, z_{un}, which can be computed by, first, determining the beamwidth of the sparse array with (2.7), θ_b. By the geometry shown in Figure 2.9, z_{un} can be computed by $z_{un} = 2R\tan\left(\frac{\theta_b}{2}\right) \approx R\theta_b$ using a small-angle approximation. For the explored "Array 2" configuration using the data with 8 passes, the average "element spacing" or baseline between successive passes, is approximately 45m. The range, R, from the phase center of array is estimated using a pass close to the center of the array, Pass 5, to be approximately 10.1 km. This results in a beamwidth of 0.00443° and a z_{un} of 0.782m.

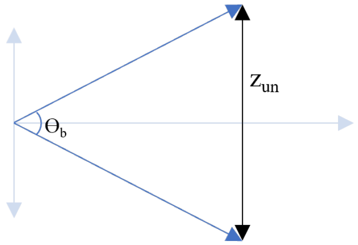

Figure 2.9: Geometry used to compute the unambiguous height, z_{un}

Chapter 3

Phase Calibration Algorithms on a Simulated Scene

The concept and mathematical basis for each of the three different data-driven phase calibration algorithms selected are discussed in this section. These algorithms are demonstrated on simulated data, first, for a sample from each element of an uncalibrated 8-element ULA, previously discussed in section 2.1.2. By viewing the element samples to be equivalent to collocated pixels in multi-pass SAR images, each of the algorithms are then applied across all collocated pixels of an uncalibrated stack of SAR images of a simulated scene. Subsequently, IFSAR processing, as previously shown in Figure 2.6, is used to resolve the relative height of the scatterers given the calibrated SAR images from each algorithm.

The simulated scene consists of 3 point scatterers, located at the following local East, North, Up Cartesian coordinates: (x_1, y_1, z_1) = (0m, 0m, 1m), (x_2, y_2, z_2) = (3m, -5m, 3m), and (x_3, y_3, z_3) = (-5m, 5m, 6m). Here, x is the ground range, y is the cross range, and z is the altitude. Simulated scatterers have an amplitude of 1. The receiver is operating at 9.6 GHz with a bandwidth of 640 MHz. Phase history data for 8 passes, at different elevations, are simulated with the collection geometry in Figure 3.1. The passes correspond to elevation angles from 0° to 0.8°. The backprojection algorithm is used to generate the SAR image at each pass. Pass 1 with elevation angle 0.8° is shown in Figure 3.2.

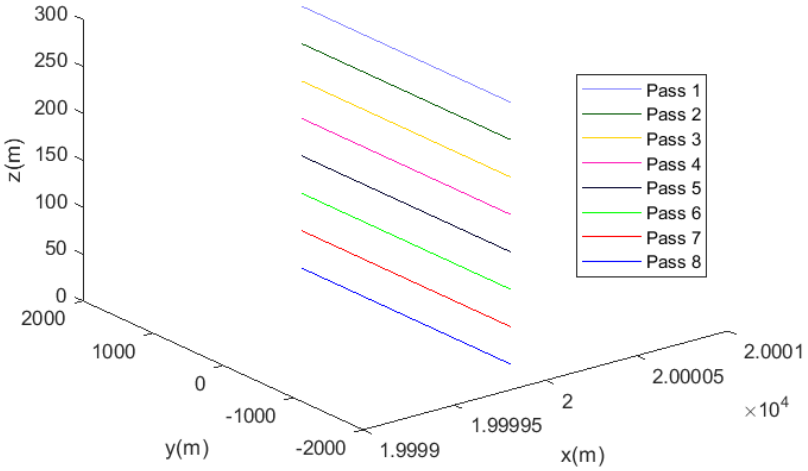

Figure 3.1: Collection geometry for simulated data

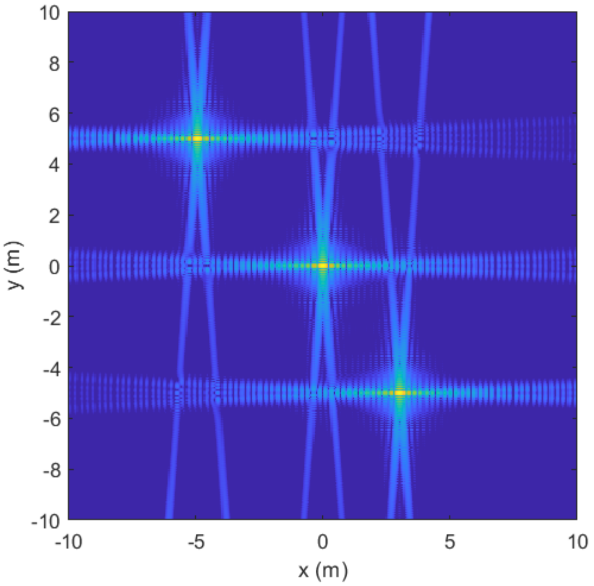

Figure 3.2: SAR image of the simulated scene generated with data from Pass 1

Figure 3.3 shows relative height map result from IFSAR processing with phase calibrated SAR images, where peak of the scatterers in the relative height map corresponds to its simulated altitude.

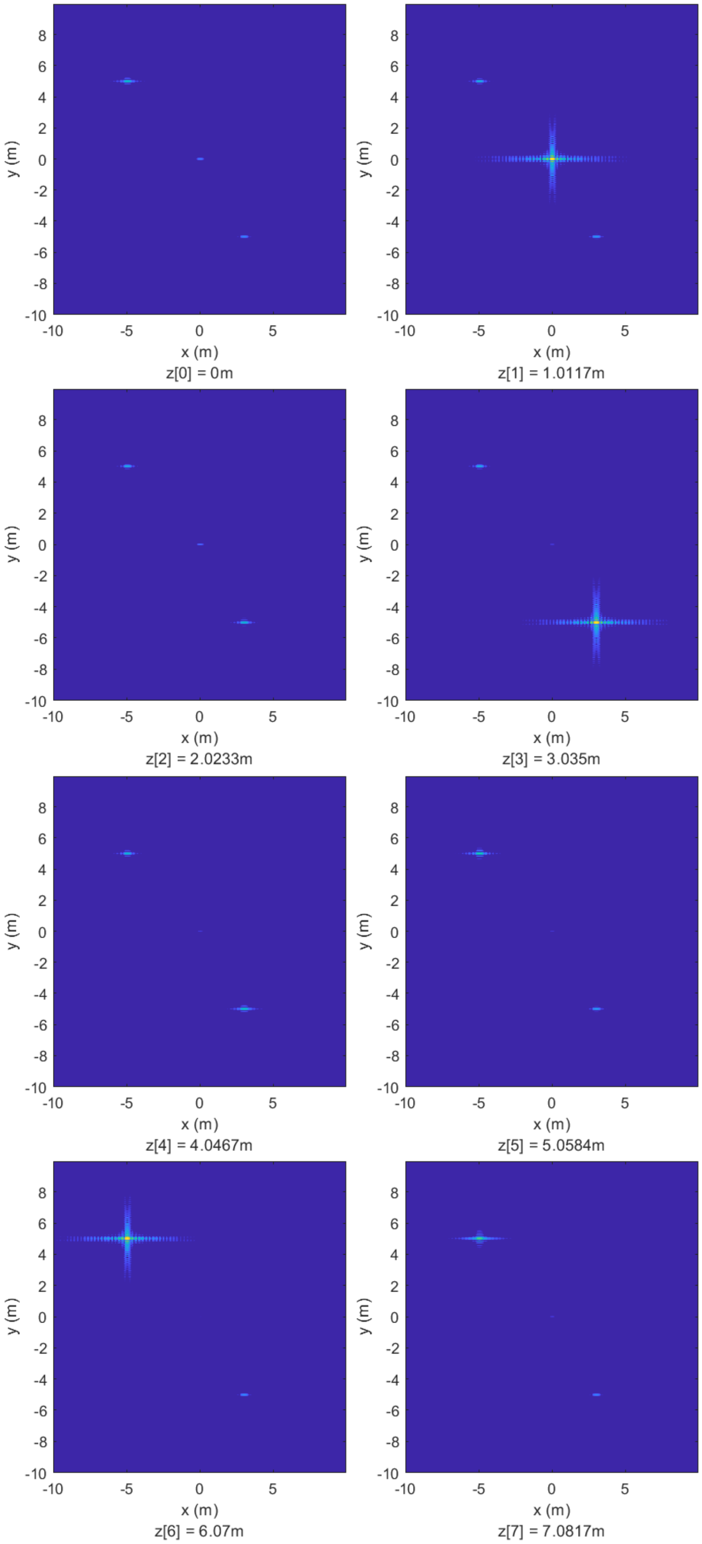

Figure 3.3: Relative height map, IFSAR processed using calibrated SAR images

Since the synthetic aperture is observing the scene from the ground, there are no layover or foreshortening effects. These effects can be seen by elevating the synthetic aperture to obtain the collection geometry by 6 km and simulating the scatterers with $x = 0$: (x_1, y_1, z_1) = (0m, 0m, 1m), (x_2, y_2, z_2) = (0m, -5m, 3m), and (x_3, y_3, z_3) = (0m, 5m, 6m). The new collection geometry for the 8 passes now correspond to elevation angles ranging from 16.7° to 17.4°, as shown in Figure 3.4.

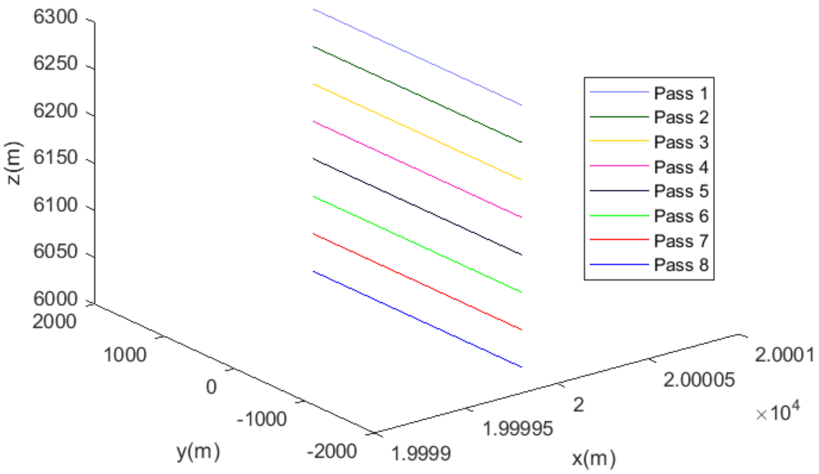

Figure 3.4: Increased elevation angles and height of the synthetic aperture for simulated data for a new collection geometry to demonstrate foreshortening effects

The resulting relative height map of this data after IFSAR processing is shown in Figure 3.5, where it is evident that the scatterers are no longer located at $x = 0$ due foreshortening effects and orthorectification is needed to correct their ground range. Of note, it is observed that by increasing the elevation angle of the passes, scatterers resolve to a taller elevation. This is especially evident for the tallest point scatterer, (x_3, y_3, z_3). This can be explained by considering the simple two look angle IFSAR geometry with (2.17) and (2.19). Using the approximation of

$$\Delta R \approx -B \sin(\varphi - \alpha) \tag{3.1}$$

the resolved elevation, z from (2.19), can be rewritten as

$$z(x,y) \approx H - R(x,y)\cos\left(\sin^{-1}\left(\frac{\Delta R}{-B}\right) + \alpha\right) \tag{3.2}$$

and

$$z(x,y) \approx H + R(x,y)\frac{\Delta R}{B} \tag{3.3}$$

where $\alpha = 0$ for a vertical interferometer. By only increasing the altitude of the synthetic aperture, ΔR increases, resulting in an increase in the resolved scatterer height.

For simplicity, the collection geometry of Figure 3.1 is used to demonstrate the effects of phase errors on the resulting relative height map. To accomplish this, phase variation following a normal distribution with a mean of 0 radians and a standard deviation of $\frac{\pi}{2}$. Additive white Gaussian noise (AWGN) with variance, σ^2 = 0.01, are added to the SAR images for each pass. The relative height map, generated with uncalibrated SAR images, is shown in Figure 3.6, showing point scatterers that are no longer focused to one altitude, demonstrating the effects of poor gain and high sidelobes in beamforming. This supports the need for phase calibration as the phase incoherency between the SAR images will result in inaccurate height estimation after IFSAR processing.

In the ideal case, after applying the phase calibration algorithms to the uncalibrated SAR images, IFSAR processing will result in Figure 3.3. However, to quantify the robustness of the algorithms, they are tested against varying levels of AWGN present in the data. Monte Carlo simulations are performed to measure the root mean square calibration error (RMSE) with respect to noise level. This is explored in section 3.4.

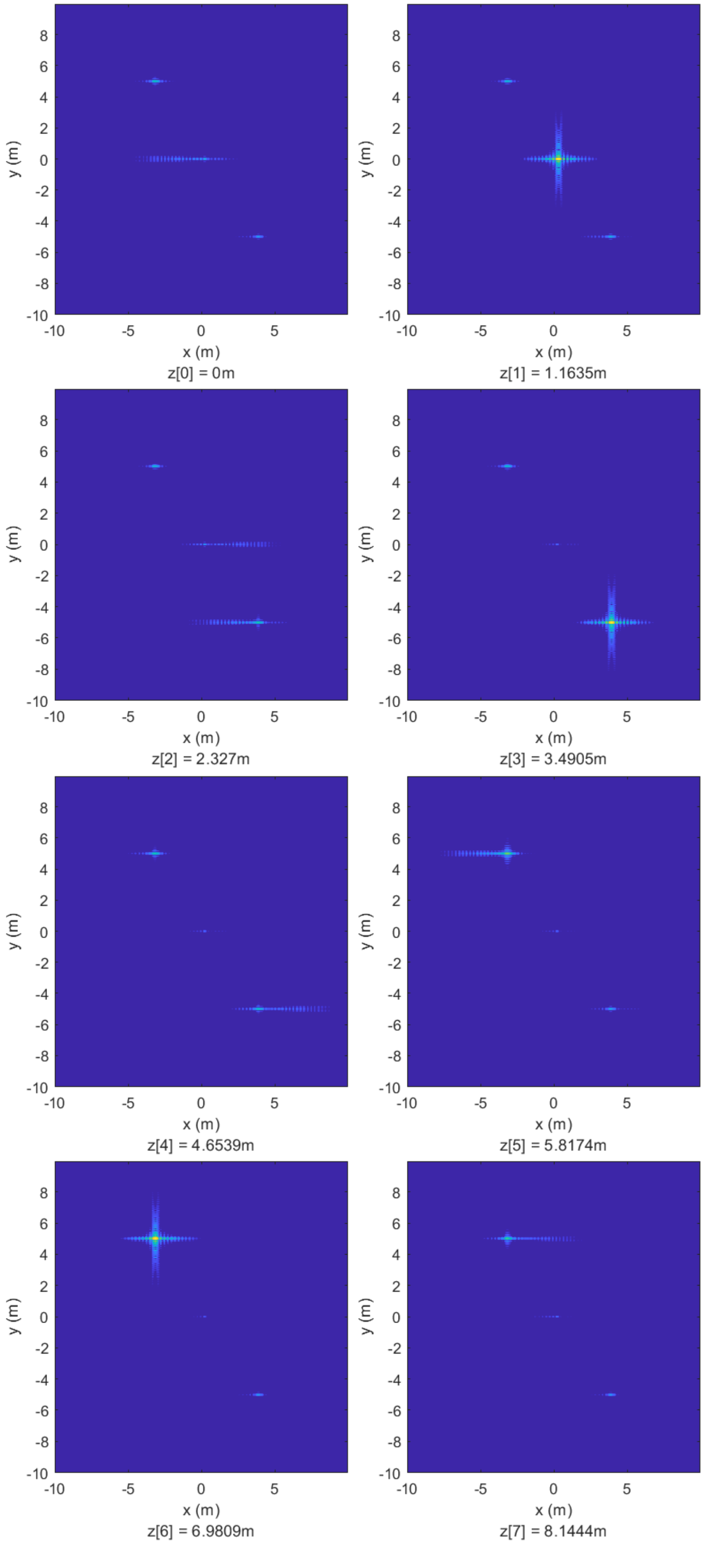

z[0] = 0m

z[1] = 1.1635m

z[2] = 2.327m

z[3] = 3.4905m

z[4] = 4.6539m

z[5] = 5.8174m

z[6] = 6.9809m

z[7] = 8.1444m

Figure 3.5: Relative height map with foreshortening effects, IFSAR processed using calibrated SAR images

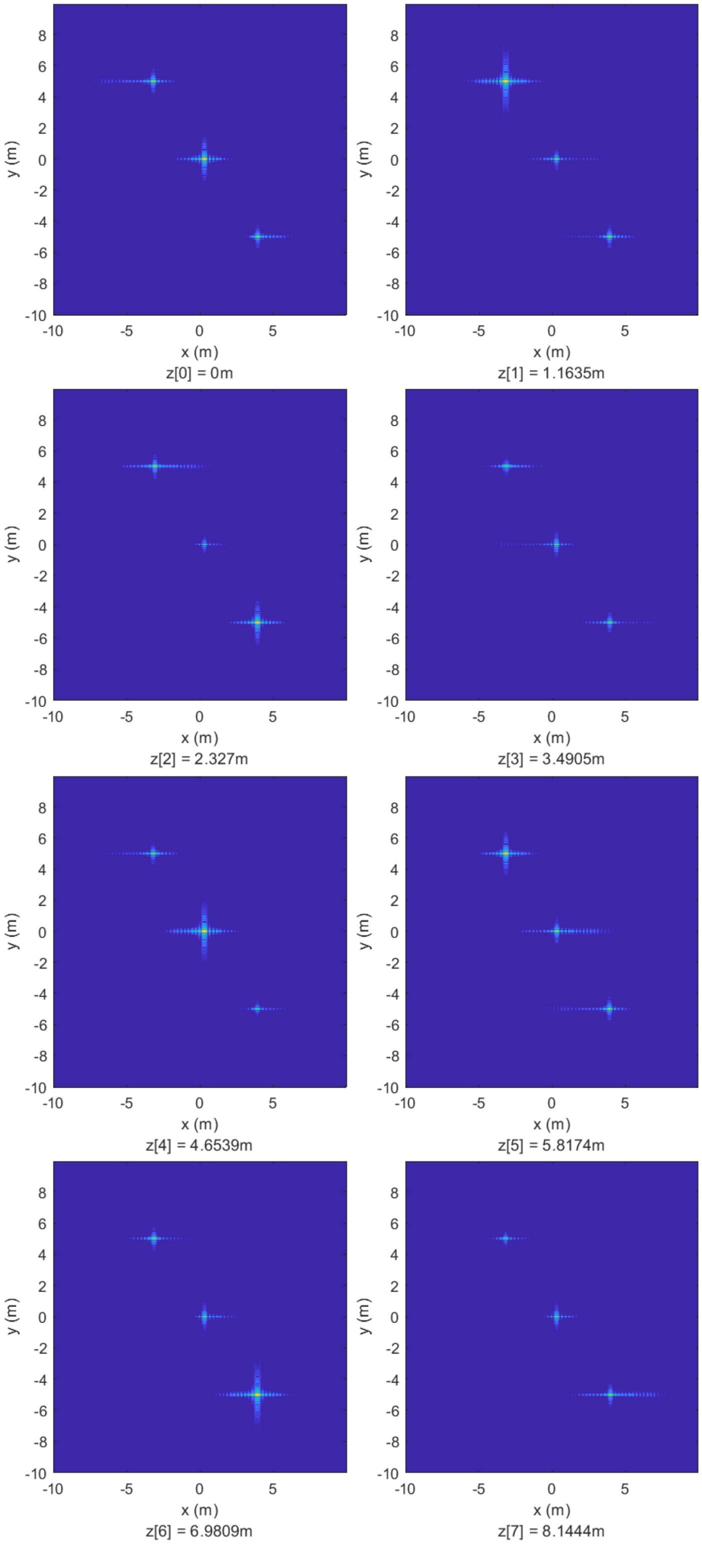

Figure 3.6: Relative height map, IFSAR processed using uncalibrated SAR images

3.1 Algorithm 1

The first algorithm is from [6], which is most similar to the classical calibration method of using a far field source from a known location. The method of [6] leverages high-SNR targets of opportunity with their location data obtained from GPS as the far field sources. The calibration vector for each source location is computed. The authors compared several methods of using the set of calibration vectors to achieve the optimal calibration performance. The averaging method, which computes the mean of all of the calibration vectors collected, is implemented for the measured SAR data. For the simulated data, one of the scatterers is used as the far field source. Pseudo-code for the averaging calibration algorithm is shown in Algorithm 1.

Algorithm 1 Calibration using High SNR Targets of Opportunity and Averaging Method

```
Input: $\vec{I}$, $d$, $\lambda$, $\vec{\theta}$, $N$, $M$
Output: $\vec{c}$
procedure AveragingCal
    for m = 1 to M do
        Select reference $I_m(1)$
        for n = 2 to N do
            $\phi_n = \frac{-j(n-1)2\pi d sin(\theta_m)}{\lambda}$
            $\beta_n = \frac{I_m(1)}{I_m(n)e^{-j\phi_n}}$
        end for
        $c_m = \vec{\beta}$
    end for
    $\vec{c} = \overline{c_m}$
end procedure
```

Figure 3.7 demonstrates the result of the algorithm on an 8-element array ULA, equivalently, 8 collocated pixels in the SAR image data stack. Uncalibrated data for each element, consisting of added phase errors and noise, are simulated across a -90° to 90° field of view. Data from 3 far field sources, located at 10°, -20°, and 30°, are simulated and used for the calibration sources. The result shown is consistent with the expected, demonstrating an increase in gain, increase in steering angle accuracy, and decrease in sidelobe levels after calibration.

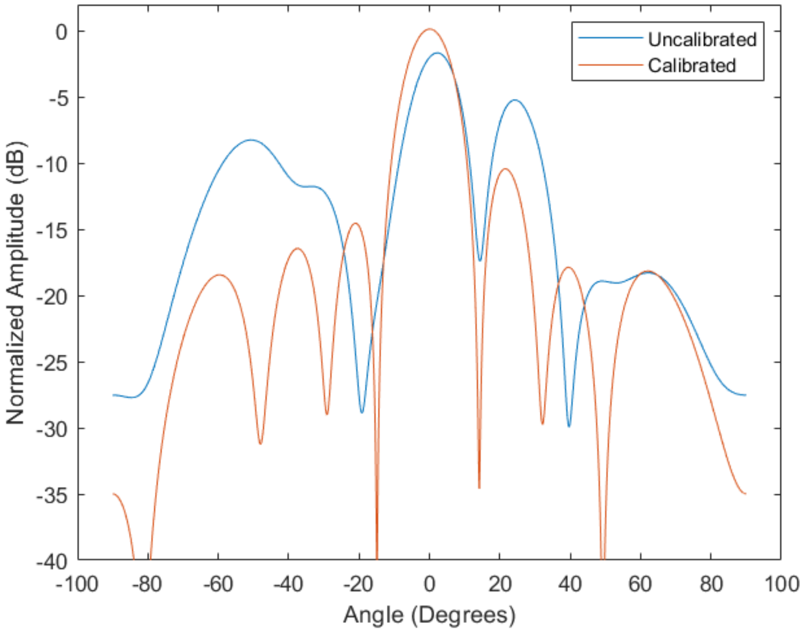

Figure 3.7: Uncalibrated and calibrated beam for an 8-element ULA using Algorithm 1

The algorithm is then extended to calibrate 8 passes of the simulated scene, as previously discussed. Here, two of the scatterers are used as the far field calibration sources. Data from these sources are used to compute the calibration coefficients. Figure 3.8 shows the resolved relative height map of the scene with the application of the calibration coefficients to all the collocated pixels in the 8 simulated SAR images, showing that the scatterers are now focused to one height and with the expected heights relative to each other. By inspection, the relative height map shows that the altitude of the scatterers are approximately 1m lower than simulated. Peak finding and applying this shift will result in the expected absolute height map.

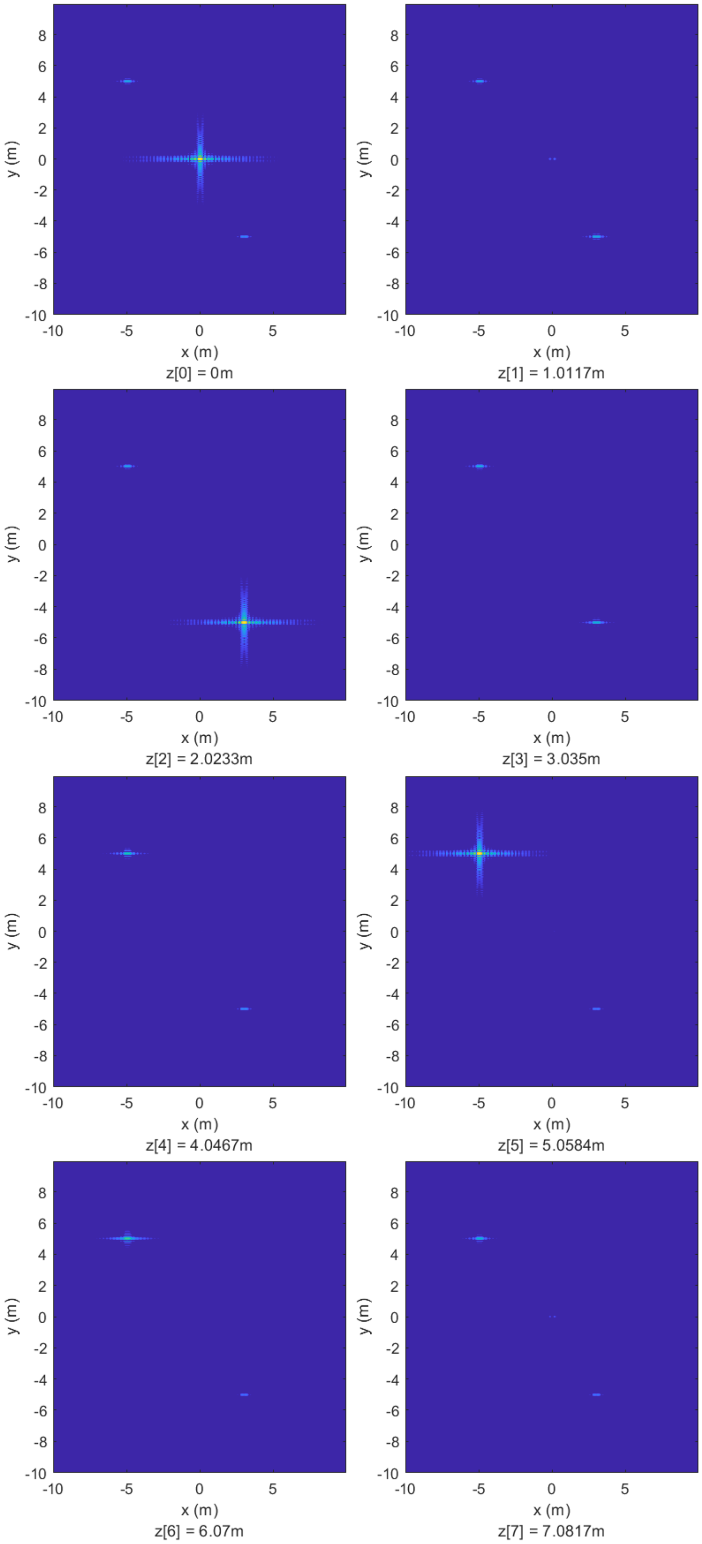

z[0] = 0m

z[1] = 1.0117m

z[2] = 2.0233m

z[3] = 3.035m

z[4] = 4.0467m

z[5] = 5.0584m

z[6] = 6.07m

z[7] = 7.0817m

Figure 3.8: Height profile of the simulated scene using data calibrated by Algorithm 1

3.2 Algorithm 2

The second algorithm is from [7] and [18] and is an optimization-based approach. Phase incoherencies defocus the beamformed data, resulting in a reduction of contrast, as observed in the height map in Figure 3.6. For this approach, phase calibrated results imply that calibration is achieved when the expected value of the contrast is maximized. Two contrast metrics, entropy and p-norm, are discussed in [7], where the entropy metric is shown to have the best overall performance, with the least residual calibration errors, on their simulated and measured data. It is also shown that calibration errors decrease with higher scene contrast or an increase in the number of range gates used.

The entropy contrast metric is selected in this work. Algorithm 2 presents the pseudo-code to maximize contrast by minimizing entropy. The entropy, E, is computed by

$$E = \sum\nolimits_{\nu=1}^{N_\nu} \frac{\vec{I_{fft}}\overline{\vec{I_{fft}}}}{\sum\nolimits_{\nu=1}^{N_\nu} \vec{I_{fft}}\overline{\vec{I_{fft}}}} \log\left(\frac{\vec{I_{fft}}\overline{\vec{I_{fft}}}}{\sum\nolimits_{\nu=1}^{N_\nu} \vec{I_{fft}}\overline{\vec{I_{fft}}}}\right) \tag{3.4}$$

where $\vec{I_{fft}}$ is the Fourier transform of the image stack $\vec{I}$ in the z dimension, $\overline{\vec{I_{fft}}}$ is its complex conjugate, $\vec{p}$ is the normalized energy, ν is the voxel index, and N_ν is the total number of voxels. The optimization is performed by leveraging Matlab functions *fft* to compute the fourier transform of the uncalibrated data, *optimset* to set the optimization parameters, and *fminunc* to compute the gradient of the entropy with respect to the calibration coefficients. Figure 3.9 demonstrates the result of this algorithm on an 8-element ULA, showing an improvement in gain, sidelobe levels, and steering angle accuracy, in the formed beam after calibration. Figure 3.10 shows that the resolved relative height map of the simulated scene after calibration of the SAR images. The scatterers have improved in contrast and are focused. They also correspond to their simulated altitudes after a shift of approximately -3m in z.

Algorithm 2 Calibration Achieved when Expected Value of Contrast is Maximized

```
    Input: $\vec{I}$
    Output: $\vec{c}$
procedure ContrastCal
$\vec{c} = \vec{0}$
    function E = EntropyFunc($\vec{c}$, $\vec{I}$)
        $\vec{I} = \vec{I}e^{j\vec{c}}$
        $\vec{I_{fft}} = \text{fft}(\vec{I})$
        $\vec{p} = \frac{\vec{I_{fft}}\overline{\vec{I_{fft}}}}{\sum_{\nu=1}^{N_\nu}\vec{I_{fft}}\overline{\vec{I_{fft}}}}$
        E = $-\sum_{\nu=1}^{N_\nu}\vec{p}\log(\vec{p})$
    end function
options = optimset('Display', 'Iter', 'TolFun', 1e-6, 'TolX', 1e-6)
$\vec{c}$ = fminunc(entropyFunc, $\vec{c}$, options, $\vec{I}$)
end procedure
```

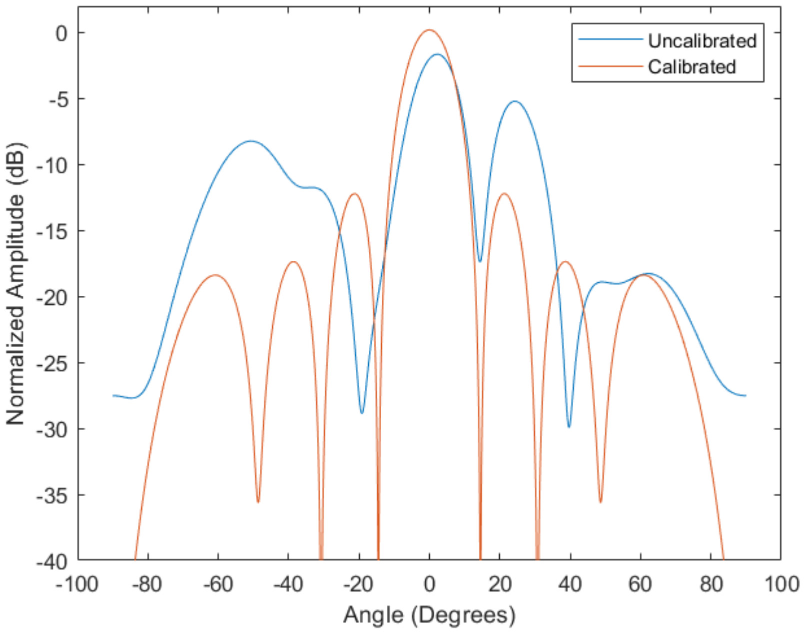

Figure 3.9: Uncalibrated and calibrated beam for an 8-element ULA using Algorithm 2

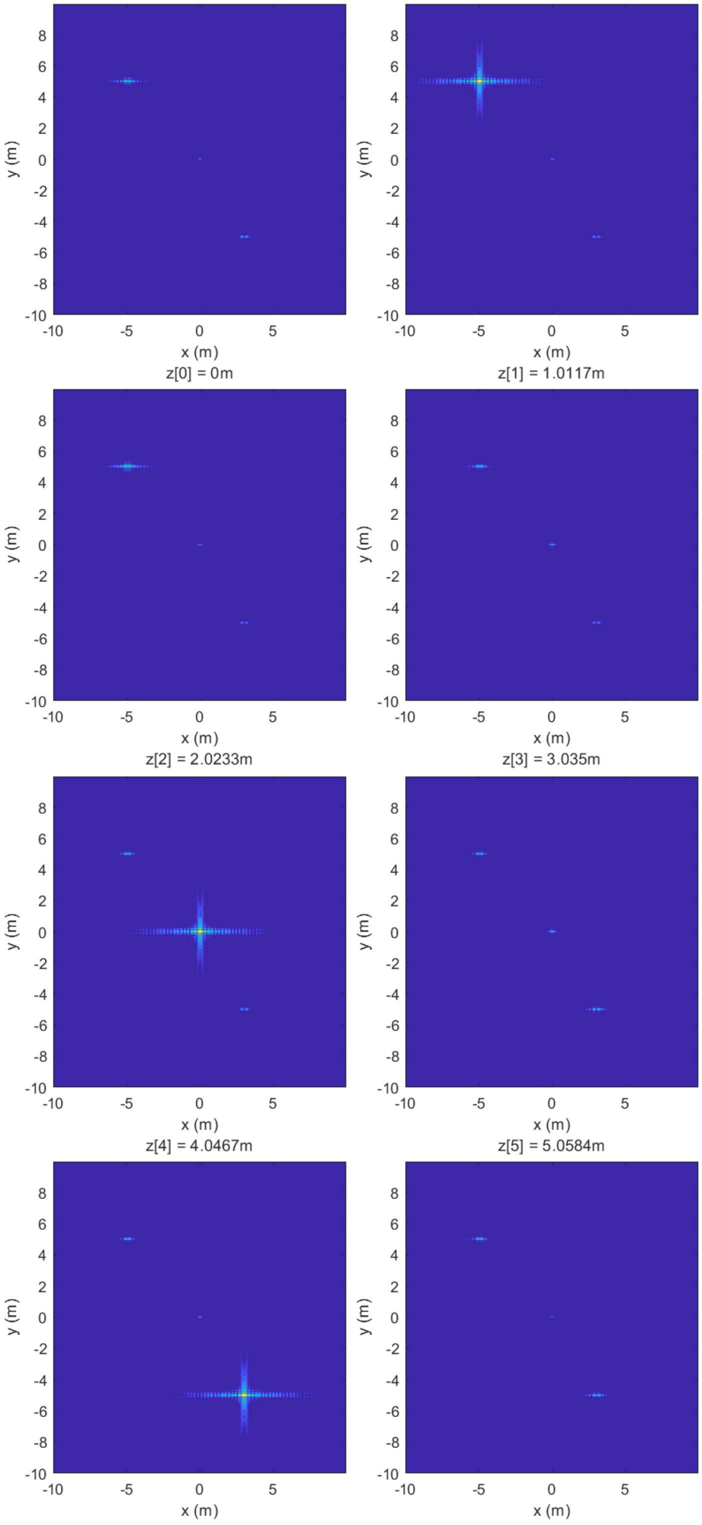

z[0] = 0m

z[1] = 1.0117m

z[2] = 2.0233m

z[3] = 3.035m

z[4] = 4.0467m

z[5] = 5.0584m

z[6] = 6.07m

z[7] = 7.0817m

Figure 3.10: Height profile of the simulated scene using data calibrated by Algorithm 2

3.3 Algorithm 3

The third algorithm is from [13], with works such as [12] demonstrating the use of this technique to calibrate a multi-channel receiver for SAR. This approach leverages the statistical properties of a homogeneous scene, from clutter or returns from noncoherent scatterers, for calibration and autocorrelating this data between successive antenna elements or SAR passes. For nonhomogeneous scenes, statistical homogenity can be accomplished by correlating over a large number of statistically similar range bins, as [13] discusses. Pseudo-code for this approach is presented in Algorithm 3.

Algorithm 3 Calibration using Clutter

```
    Input: $\vec{T}$, $N$, $\Upsilon$
    Output: $\vec{c}$
procedure CLUTTERCAL
$\vec{c} = \vec{0}$, $idx = 1$, $l = 2$, $m = 1$
    for pass = 1 to N-1 do
        for r = 1 to $\Upsilon$ do
            $acf(l, m, r) = \frac{\sum_{y=1}^{N_y} \overrightarrow{T(r,1{:}N_y,pass)} \cdot \overline{\overrightarrow{T(r,1{:}N_y,pass+1)}}}{\Upsilon}$
        end for
        $acf_{avg}(l, m) = \frac{\sum_{r=1}^{\Upsilon} acf(l,m,r)}{\Upsilon}$
        $ph[idx] = \arg\left(acf_{avg}(l, m)\right)$
    end for
    $c[idx] = -\sum_{k=1}^{idx} ph[idx]$
    Increment $idx$, $l$, and $m$ by 1
end procedure
```

A 41 x 41 clutter patch is simulated for the 8 SAR passes. These are simulated as point scatterers for x = 5m to 7m, y = 5m to 7m, and z = 1m to 3m. Figure 3.11 shows the SAR image of the scene containing the clutter patch. As with the results from the previous 2 calibration algorithms, Figure 3.12 demonstrates an improvement in gain, sidelobe levels, and steering angle accuracy for beamforming with an 8-element ULA while Figure 3.13 demonstrates focusing of the scatterers, where a shift of approximately -5m in z results in their simulated altitudes.

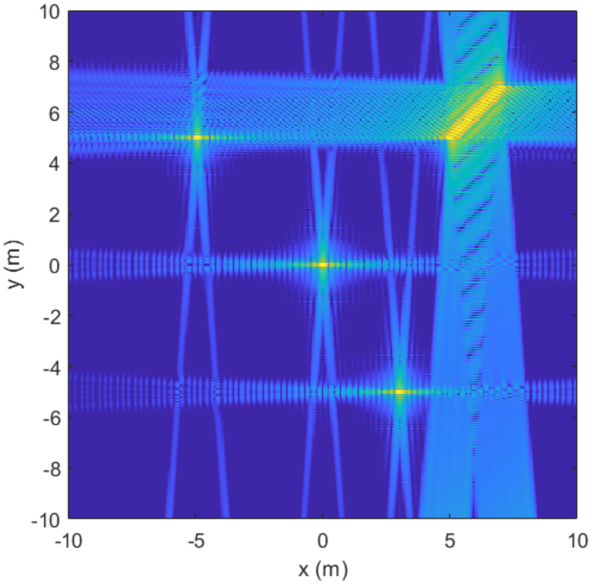

Figure 3.11: SAR image of the simulated scene with clutter (Pass 1)

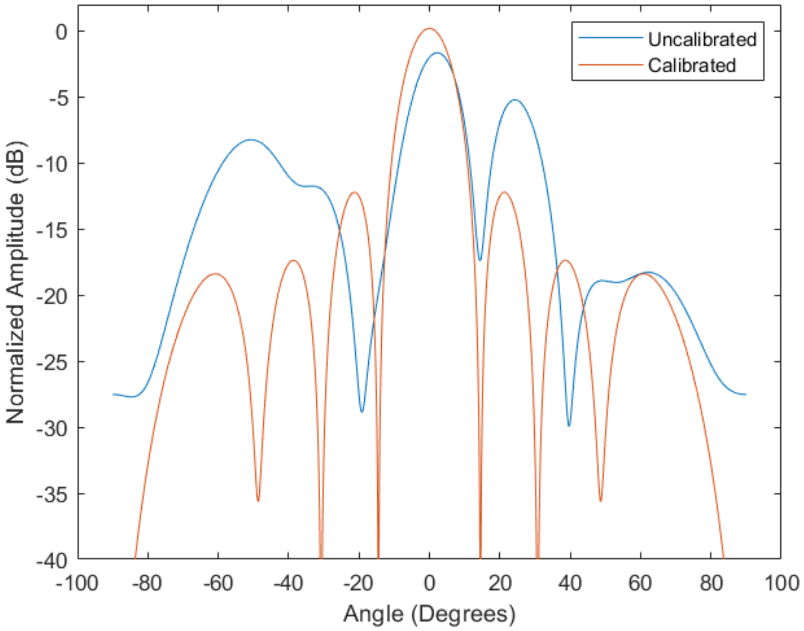

Figure 3.12: Uncalibrated and calibrated beam for an 8-element ULA using Algorithm 3

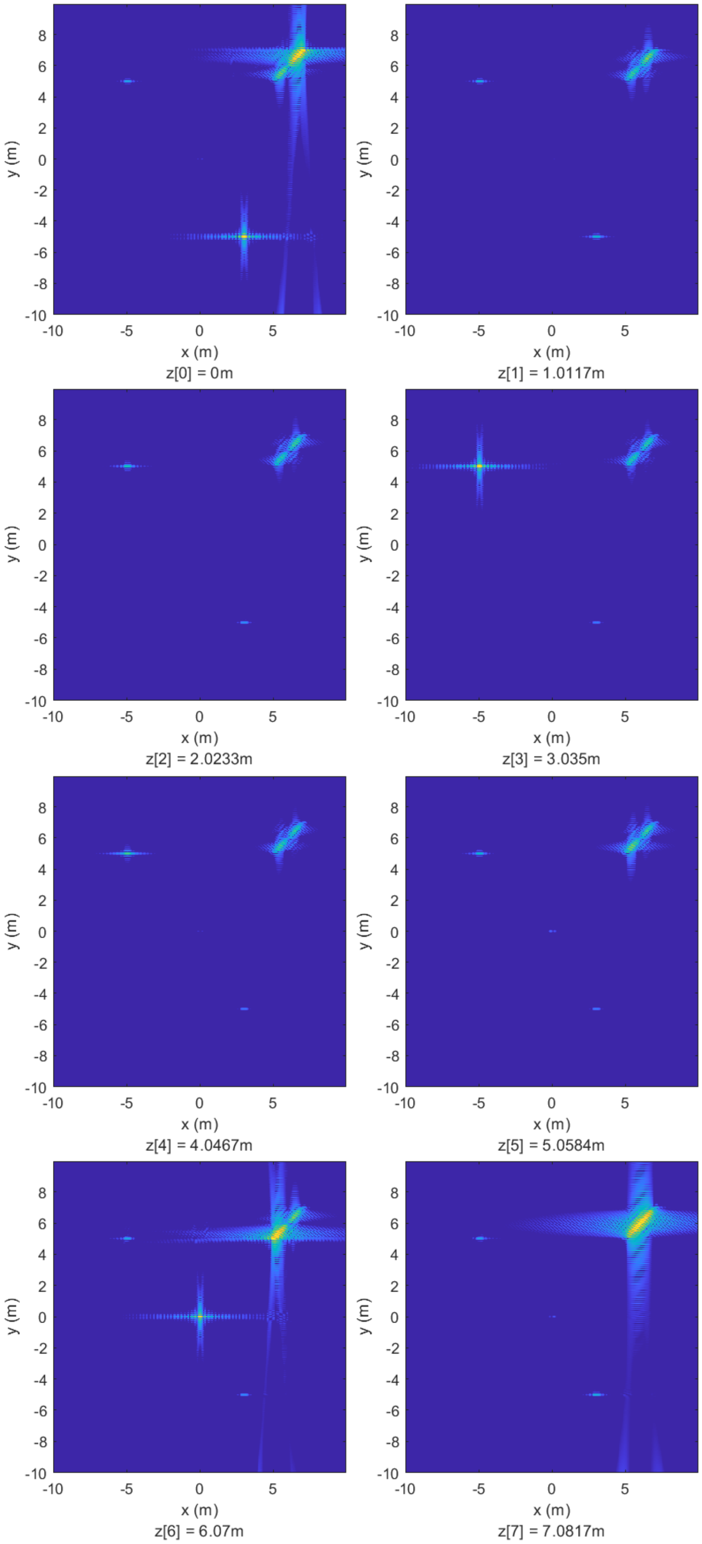

z[0] = 0m

z[1] = 1.0117m

z[2] = 2.0233m

z[3] = 3.035m

z[4] = 4.0467m

z[5] = 5.0584m

z[6] = 6.07m

z[7] = 7.0817m

Figure 3.13: Height profile of the simulated scene using data calibrated by Algorithm 3

3.4 Effect of AWGN on Calibration Errors

Monte Carlo simulation with 5000 runs is performed for each algorithm. The simulated data from the uncalibrated 8-element ULA are used for these experiments. The data has an amplitude of 1 and the added phase errors follow a Gaussian distribution with a mean of 0 radians and a standard deviation of $\frac{\pi}{2}$ radians. AWGN with variance σ^2 ranging from 0.01 to 1 is also added to the data to simulate a decrease in SNR. The residual phase errors are determined from the phase calibration coefficients from each algorithm as compared to the added phase errors. The best fit line and the mean of the unwrapped residual phase errors are determined and removed, forming $\vec{\zeta}$. The RMSE is then calculated by

$$RMSE = \sqrt{\frac{\sum_{n=0}^{N-1} |\vec{\zeta}|^2}{N}} \tag{3.5}$$

Figures 3.14, 3.15, and 3.16 show the computed RMSE for each element, with the averaged RMSE shown by the dashed line. The average RMSE under different noise levels is summarized in Figure 3.17. These figures demonstrate that there is an increase in calibration errors with the increase in noise for all algorithms. On average, the algorithms perform well given small noise variance of σ^2 = 0.01 and σ^2 = 0.05. Algorithm 1 performs best with high SNR data, since this approach leverages high SNR sources of opportunity at known angles. The averaging of the calibration coefficients from multiple sources can help the calibration performance in the presence of noise to achieve the best fit calibration vector. Algorithm 2 and Algorithm 3 have comparable performance given low levels of noise. This can be expected because high noise reduces the contrast and perturbs the statistics of the scene. As Algorithm 2 and Algorithm 3 can leverage data from the entire scene or a clutter patch respectively, more data may help to reduce the error for both of these algorithms. This is shown in [7], where the authors show a decrease in residual error with the number of range gates.

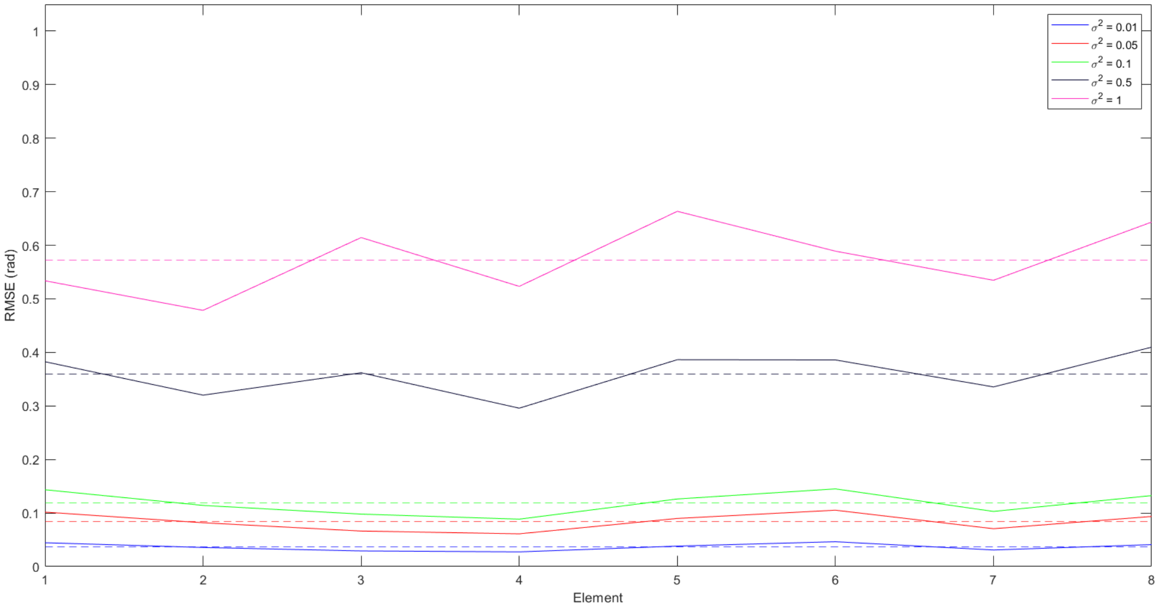

Figure 3.14: RMSE under different noise levels for Algorithm 1, with average RMSE

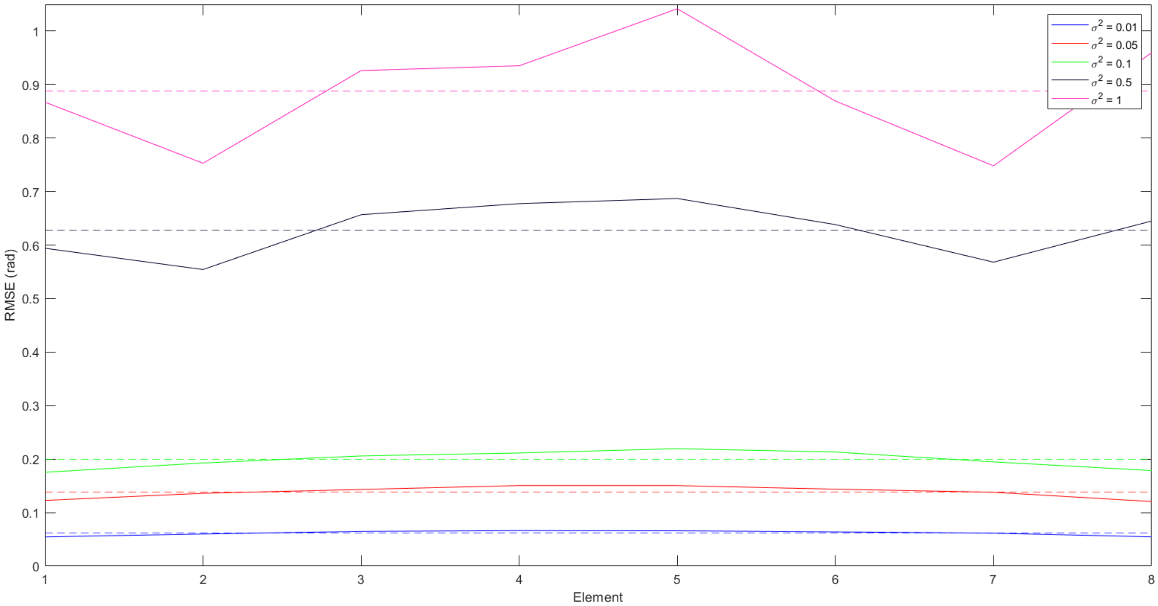

Figure 3.15: RMSE under different noise levels for Algorithm 2, with average RMSE

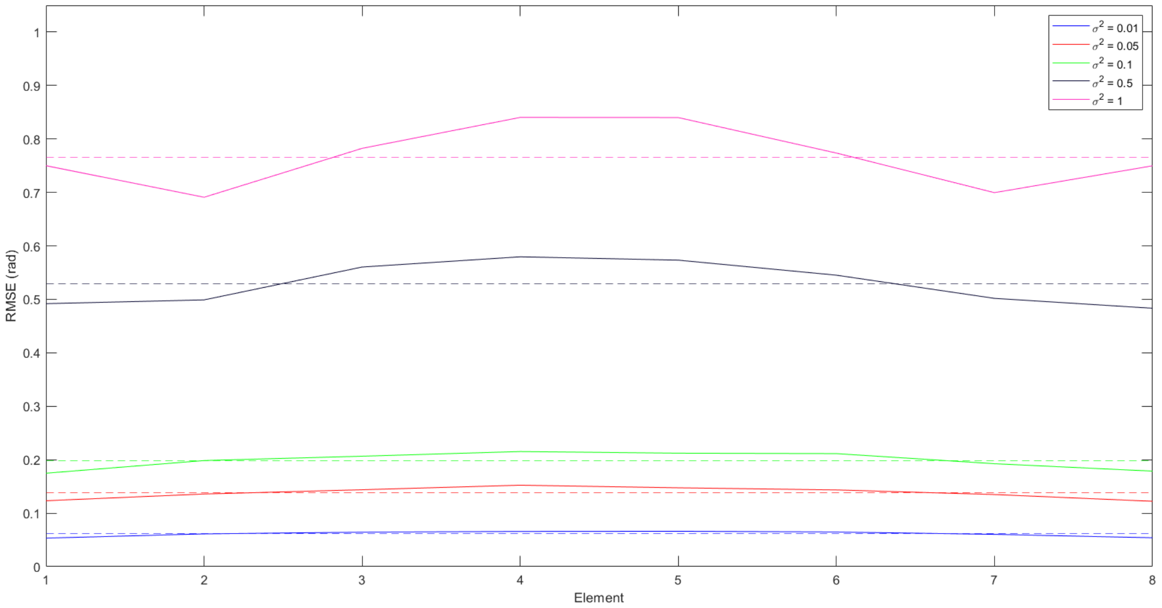

Figure 3.16: RMSE under different noise levels for Algorithm 3, with average RMSE

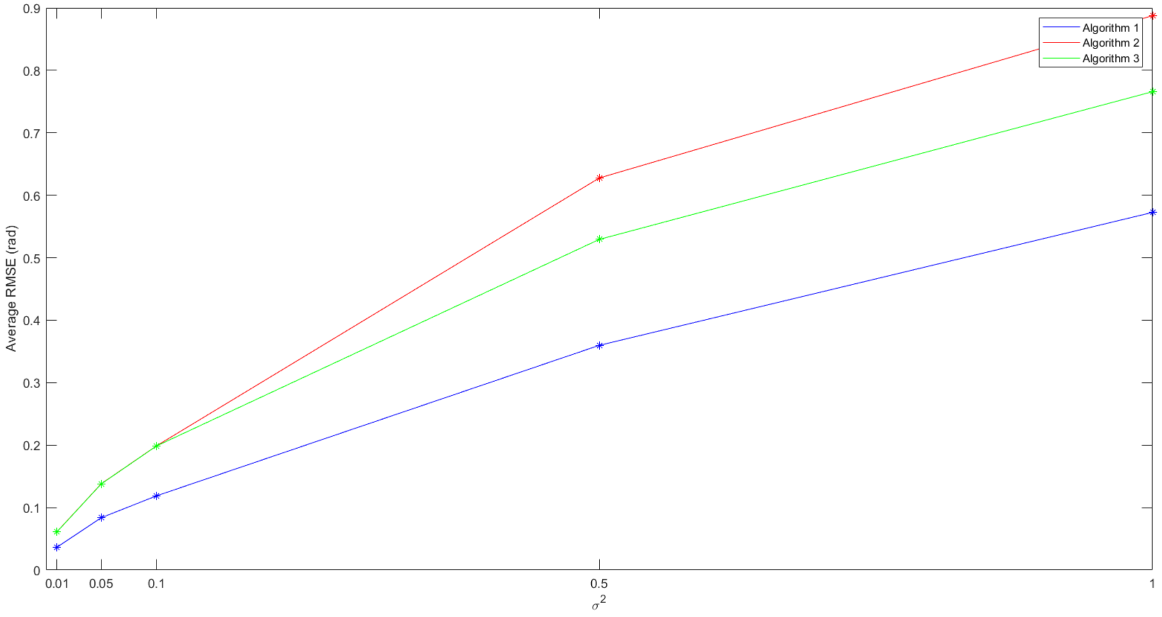

Figure 3.17: Phase calibration errors increase with the decrease in SNR, with Algorithm 1 showing best performance overall and Algorithms 2 and 3 showing higher sensitivity to noise

3.5 Simulated Algorithms Summary

Figure 3.18 summarizes the uncalibrated and calibrated beamforming results for the simulated 8-element ULA. Applying the calibration algorithms to the 8 simulated successive SAR passes have demonstrated agreement with these results. For low levels of noise, all 3 calibration algorithms provide comparable and significant improvement in beam pointing accuracy, side lobe levels, and sensitivity over the uncalibrated case. However, as the SNR of the data decreases, calibration errors increase. With low SNR, an optimization-based or clutter-based calibration algorithm may be more suitable.

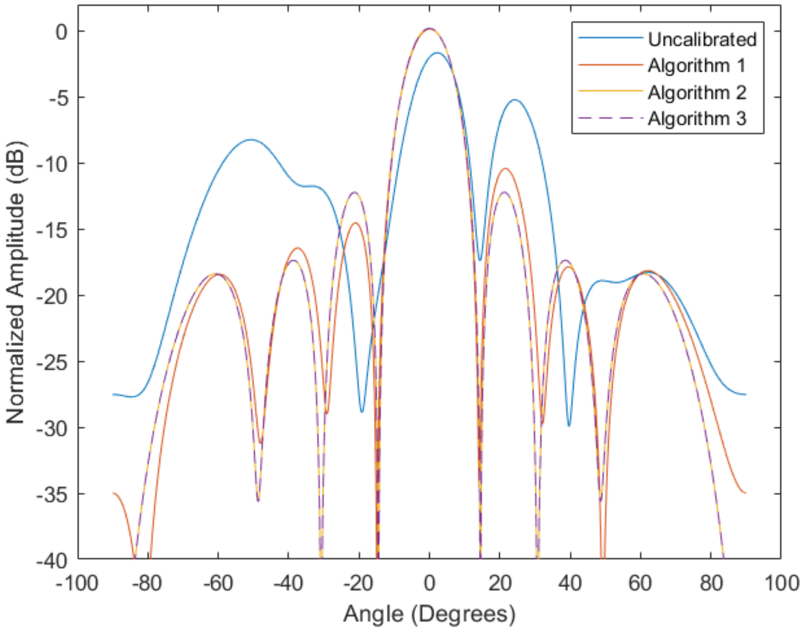

Figure 3.18: Uncalibrated and calibrated beams for an 8 element ULA by the 3 algorithms

While Algorithm 1 uses sources of opportunity with known angles of arrival relative to the synthetic aperture, Algorithms 2 and 3 do not. As a result, it is important to also consider that the calibration coefficients may contain an unknown linear phase offset, as mentioned in [7], [13], and [12]. A linear phase offset translates to beam pointing error or a shifting of the height map in altitude. This ambiguity can be corrected with a source at a known angle of arrival or a scatterer with a known height.

Chapter 4

Analysis and Results

In the previous chapter, the selected phase calibration algorithms demonstrated beamforming improvement in generating the expected height map when applied to the processing chain for simulated data with phase incoherencies. In this chapter, the calibration step and algorithms are introduced to the processing of measured data, specifically, the 8 passes in the Volumetric SAR dataset. The SAR images of the scene at each successive pass is formed by backprojecting the pulses in the phase history data for azimuth angles $42^\circ - 44^\circ$, collected in the HH polarization. After image formation via backprojection, IFSAR processing is performed via the steps in Figure 2.6.

Image registration is performed between the 8 SAR images to spatially align them in translation and rotation. The SAR images from Passes 2-8 are registered to Pass 1. Successful registration of the passes is shown in Figure 4.1. As noted in Figure 4.2, several features can be observed in the scene at these azimuth angles, including 3 trihedral calibration targets, a light pole, a top hat, roads, trees, and vehicles. The known heights of some of these objects is later used to ascertain the absolute height map of the scene.

To develop the baseline for comparing the effects of phase calibration, the relative height map is formed first without calibrating the registered SAR images. This beamformed result is shown in Figure 4.3. Here, only pixels with a measured amplitude of greater than

-45 dB are shown. By inspection, though some scatterers appear mildly stronger at certain elevations than others, overall, they are not focused in height, with their amplitudes tending to span across a wide range in elevation, making it difficult to discern their relative heights. This is observed in Figure 4.4 for a scatterer from the tophat in the scene. In general, the normalized gain is low, showing poor sensitivity. This normalization factor is kept constant and applied to height maps formed with and without calibration. In the following sections, the calibration coefficients from each of the explored phase calibration algorithms are applied to the SAR passes prior to forming the relative height maps. The resulting relative height maps are discussed.

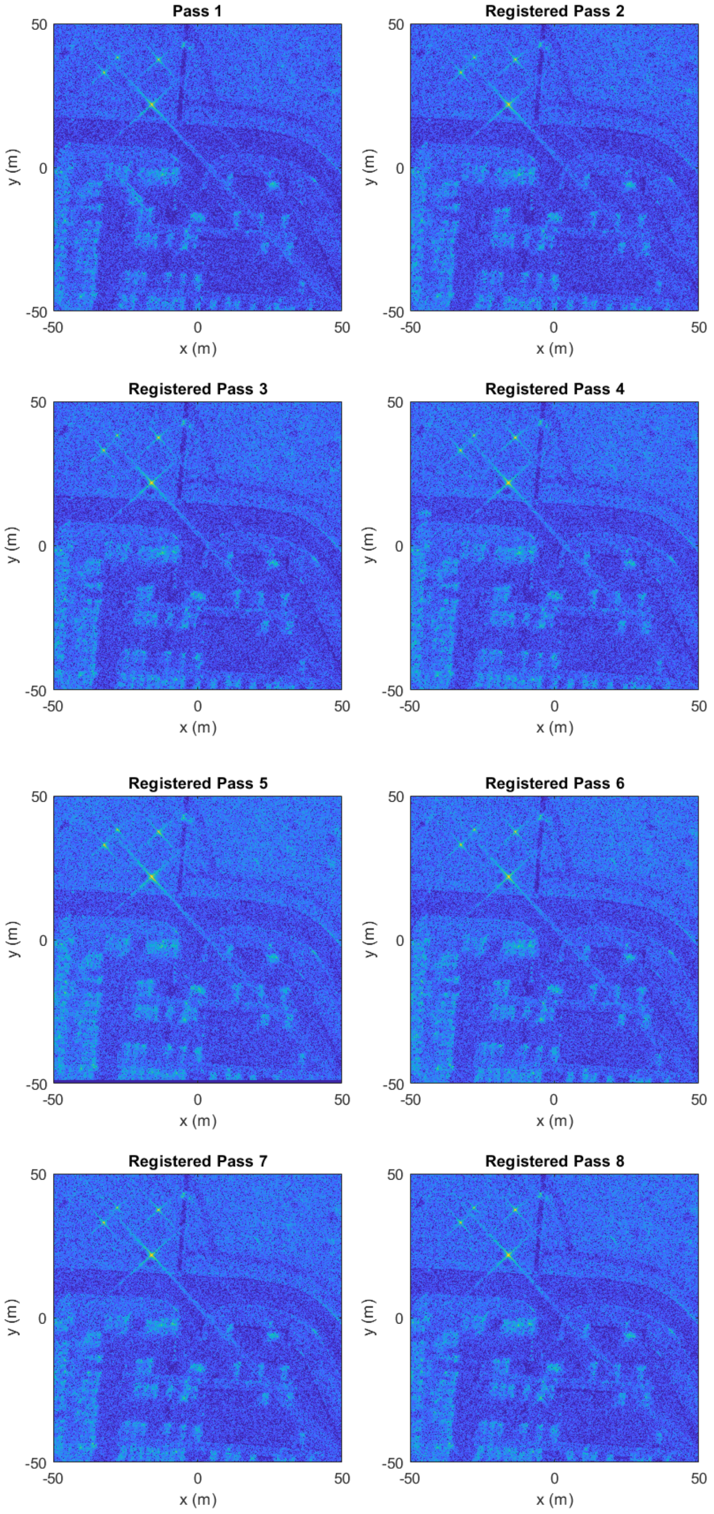

Figure 4.1: Registered images of the Gotcha scene

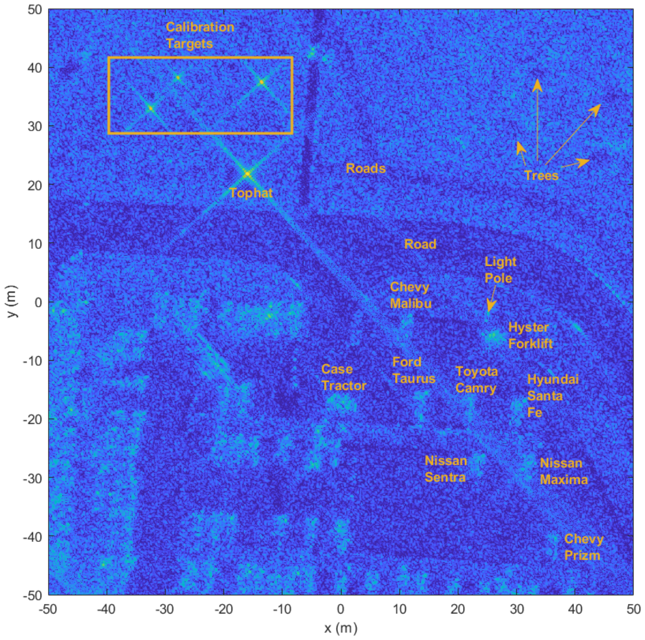

Figure 4.2: Pass 1, $42° - 44°$ azimuth, scene with labeled objects

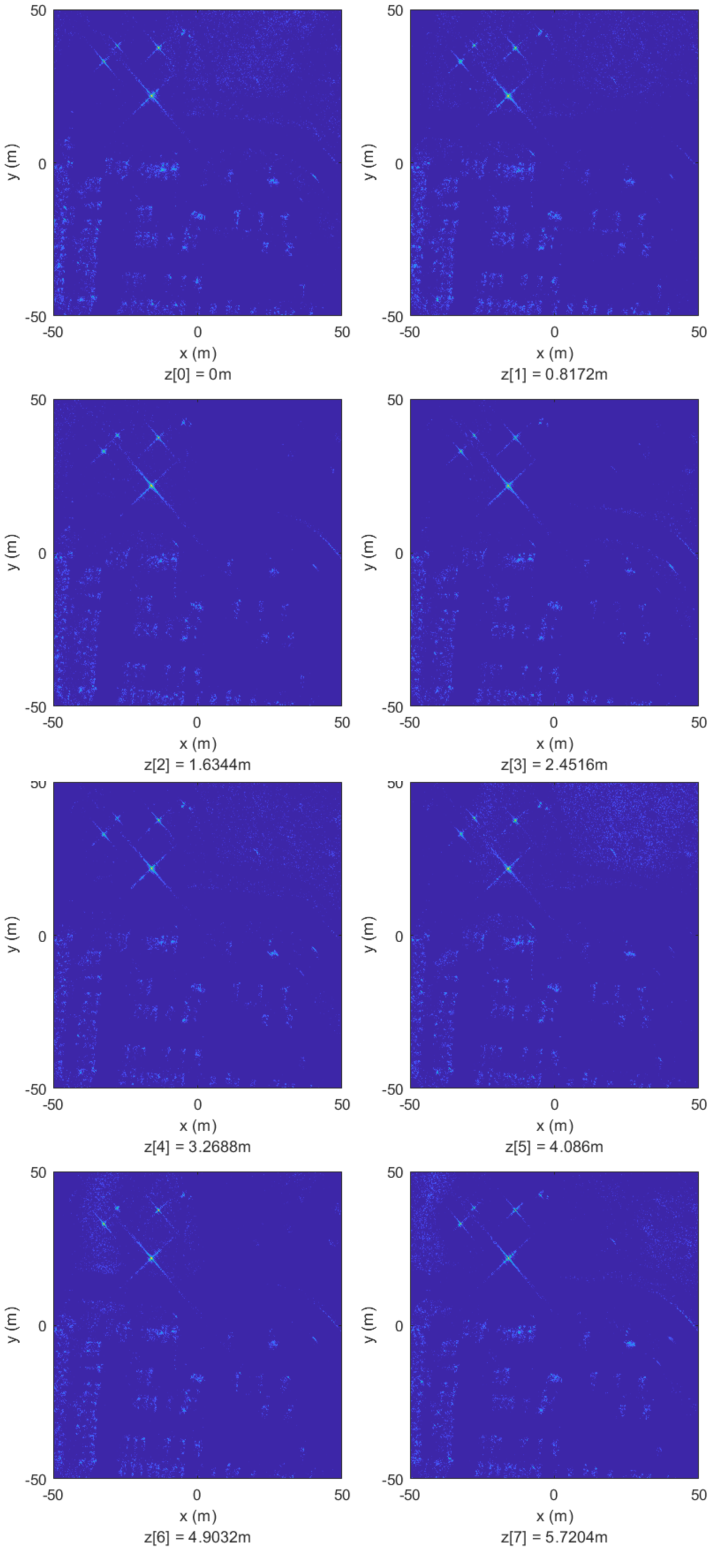

Figure 4.3: Relative height map of the Gotcha scene, without calibration of the registered SAR images

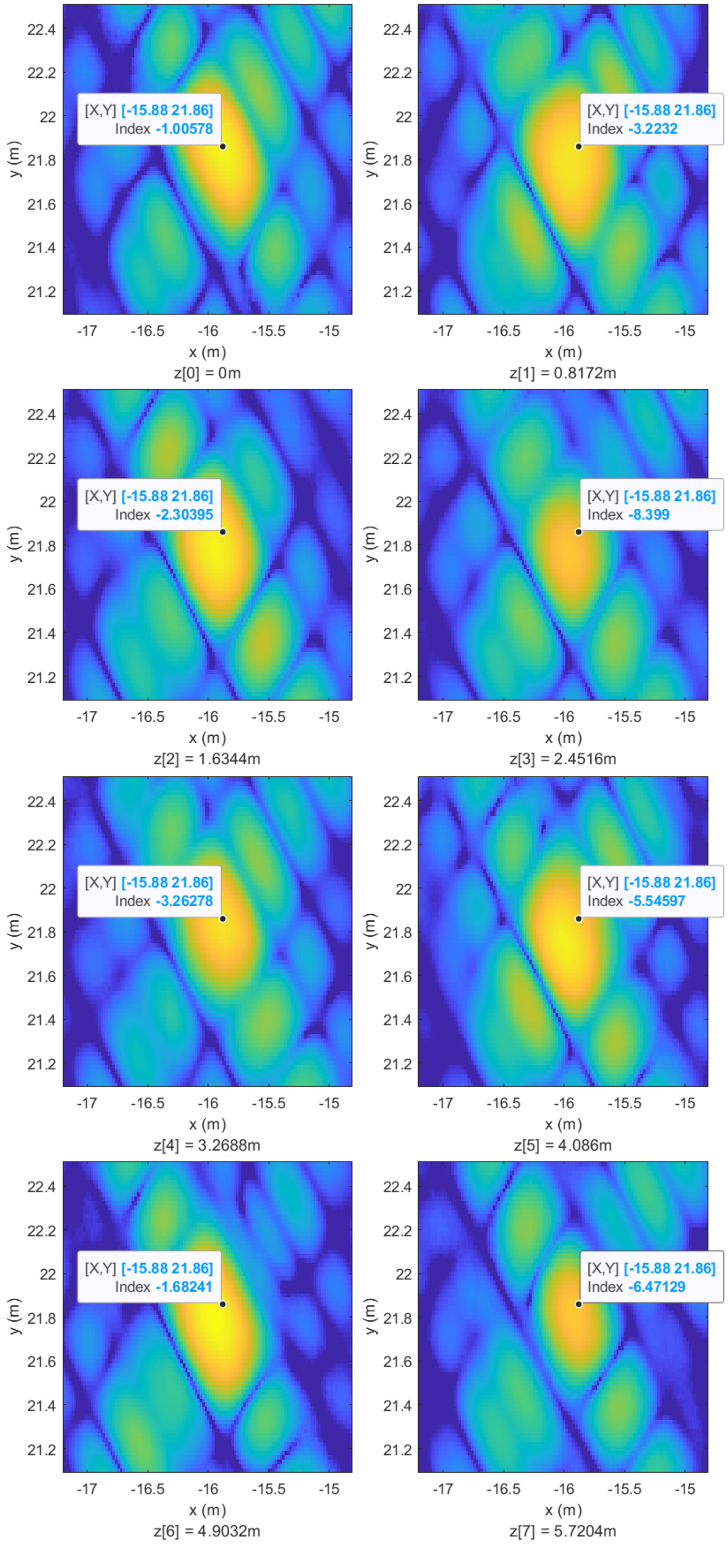

Figure 4.4: Relative height map of the tophat in the Gotcha scene without calibration of the registered SAR images

4.1 Phase Calibration Algorithms on Measured Gotcha Volumetric SAR Data

4.1.1 Algorithm 1

The 3 trihedrals in the top left of the scene are convenient scatterers of opportunity to be used as calibration sources. Phase calibration coefficients are computed for each source. The phases are unwrapped and averaged to obtain the final calibration vector. While there seems to be a trend in the coefficients, Figure 4.5 shows some non-convergence. Multipath and noise may have contributed to this discrepancy. Returns from the calibration sources at different locations can experience different signal interaction with the objects in the scene and cause variations in the phases observed at the sensors. Furthermore, this algorithm is more sensitive to noise. Hence, averaging the calibration vectors from several sources to calibrate the SAR images may improve the overall performance of the beamformed result.

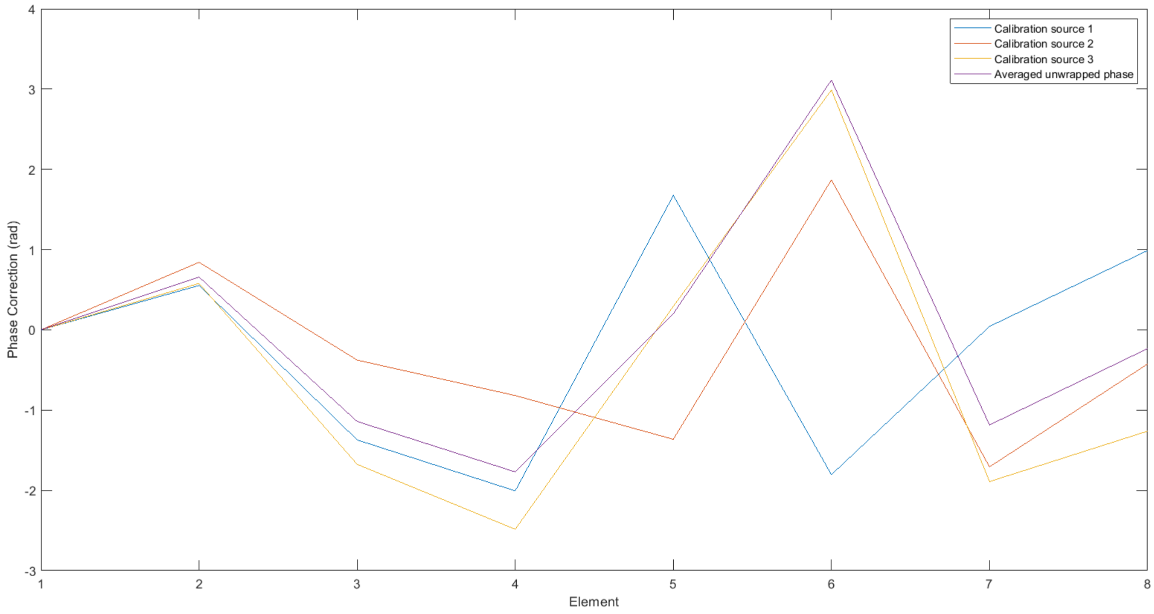

Figure 4.5: Phase calibration coefficients from each calibration source with the averaging of the unwrapped phase

The resulting relative height map after applying the averaged calibration coefficients to the SAR images and performing IFSAR processing with multiple look angles, as previously described, is shown in Figure 4.6. Figure 4.6 demonstrates an improvement in the sensitivity and focusing of the scatterers in elevation after calibration, where it is seen that different sections of the scene appear focused to different elevations. This is most evident when observing the $z[0]$, $z[1]$, $z[6]$, and $z[7]$ elevation slices. Compared to the uncalibrated relative height map, the roads as well as vehicles can now be seen more prominently. Furthermore, the gain improvement is evident from analyzing the amplitude of the scatterers. Figure 4.7 shows the tophat, now peaking at an amplitude of 1.75 dB after calibration.

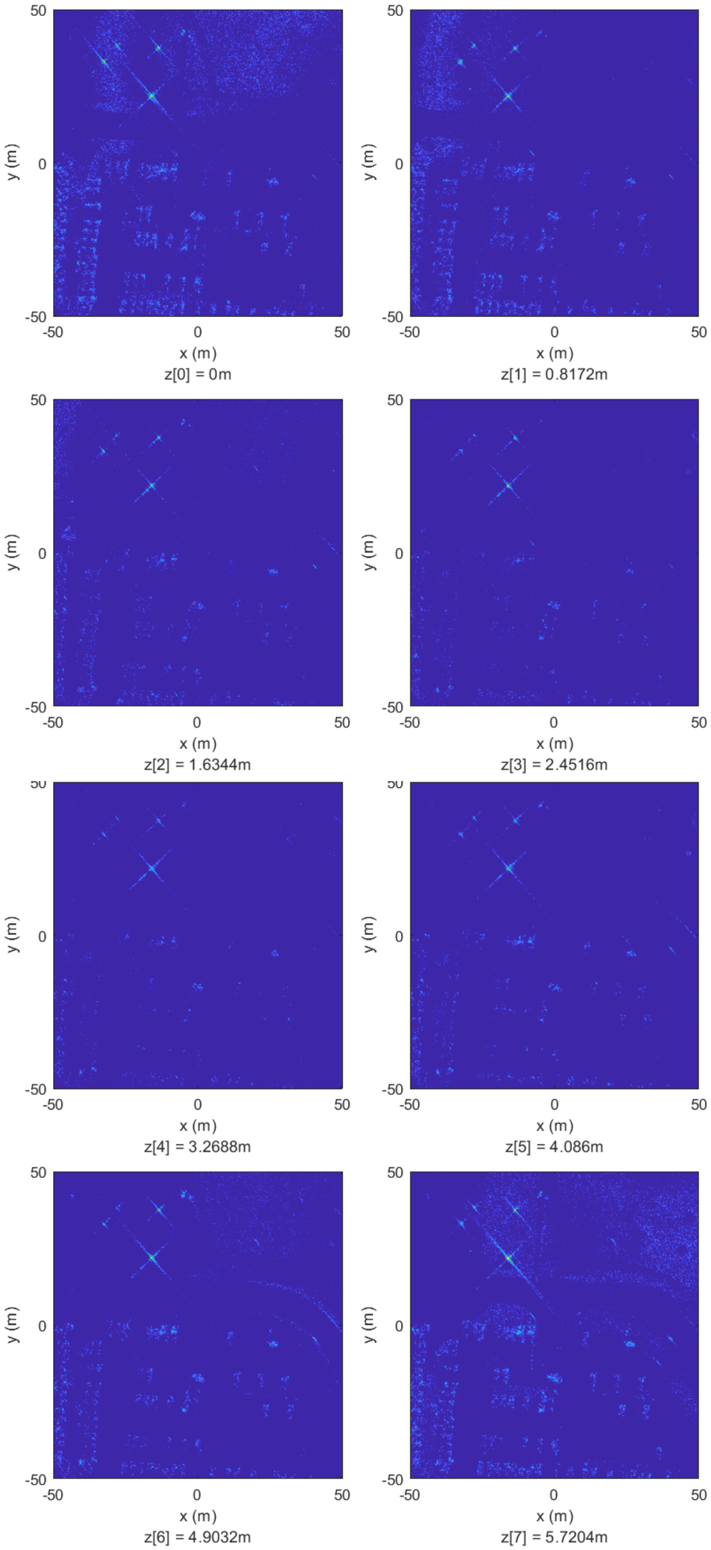

z[0] = 0m

z[1] = 0.8172m

z[2] = 1.6344m

z[3] = 2.4516m

z[4] = 3.2688m

z[5] = 4.086m

z[6] = 4.9032m

z[7] = 5.7204m

Figure 4.6: Height profile of the Gotcha scene, using data calibrated by Algorithm 1

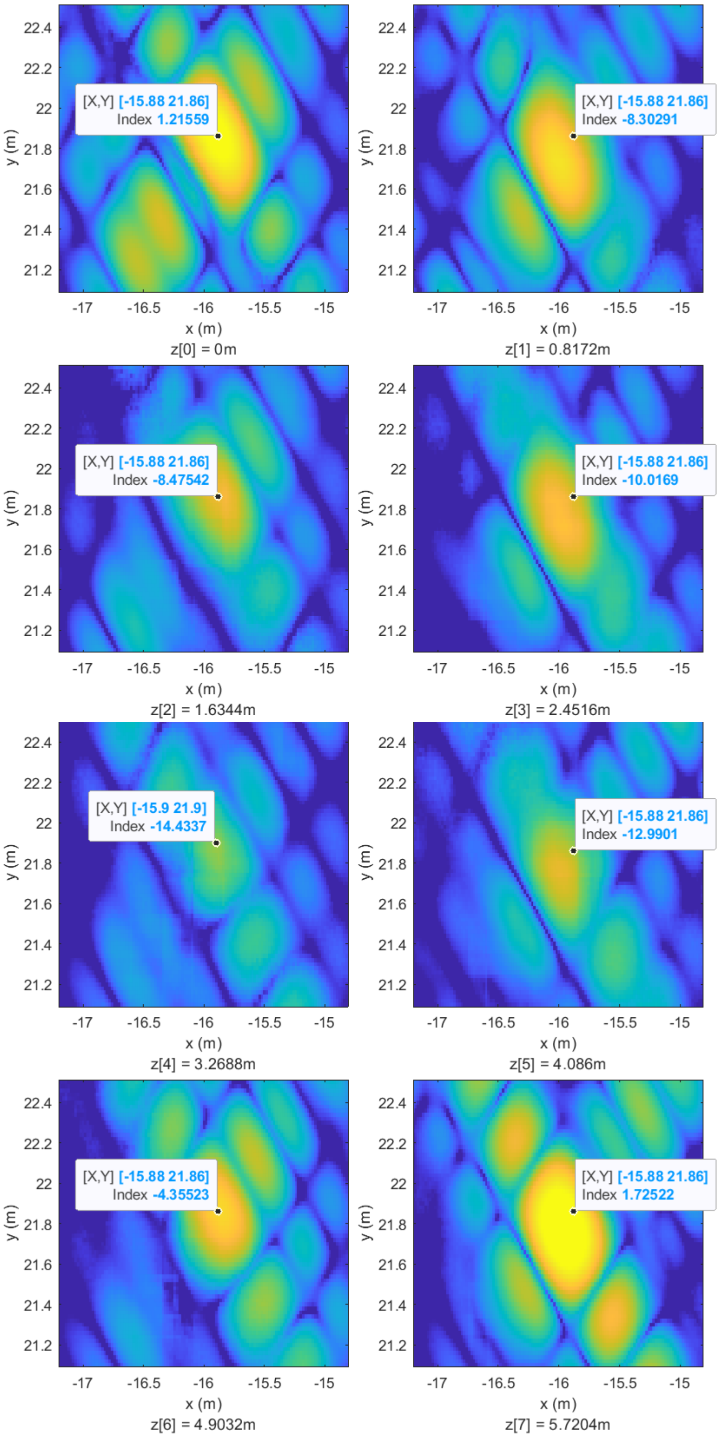

z[0] = 0m

z[1] = 0.8172m

z[2] = 1.6344m

z[3] = 2.4516m

z[4] = 3.2688m

z[5] = 4.086m

z[6] = 4.9032m

z[7] = 5.7204m

Figure 4.7: Height profile of the tophat in the Gotcha scene, using data calibrated by Algorithm 1

4.1.2 Algorithm 2

For contrast-based calibration, optimization is performed to minimize the entropy of the beamformed result. The phases of the full, registered, but uncalibrated SAR images are extracted and the gradient of the entropy function with respect to the calibration coefficients are iteratively computed until the convergence criteria is met. The convergence criteria is met when the gradient is less than the optimality tolerance of 10^{-6}. The resulting relative height map is shown in Figure 4.8, with the zoomed in section of the tophat shown in Figure 4.9. After calibration, an improvement in the sensitivity and the focusing of the scatterers across elevation is observed. The roads can be clearly identified and vehicles can be seen to be peaking stronger at certain elevations. The improvement in gain is also evident by inspecting a scatterer from the tophat of Figure 4.9. The scatterer is focused to one altitude, $z[1]$, with a peak amplitude of 3.22 dB.

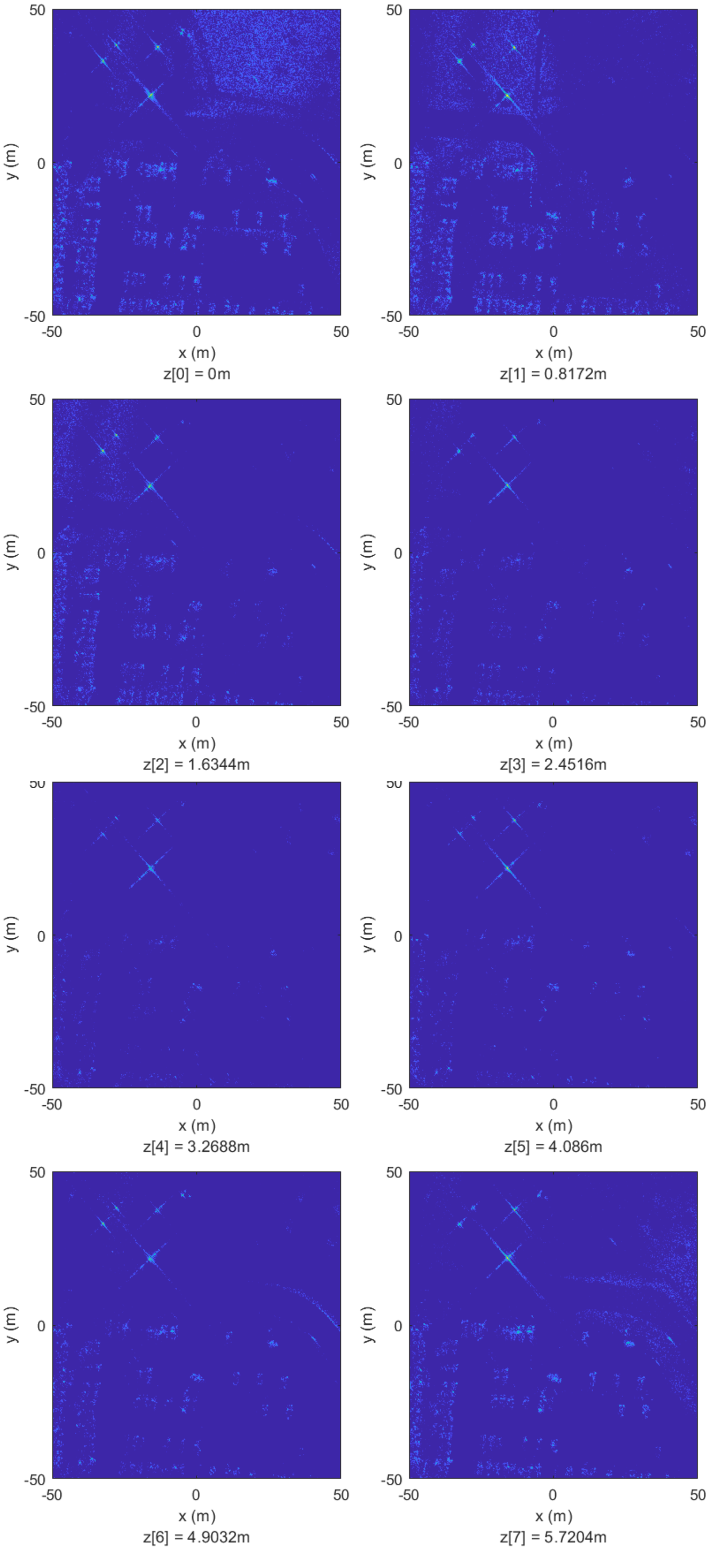

z[0] = 0m

z[1] = 0.8172m

z[2] = 1.6344m

z[3] = 2.4516m

z[4] = 3.2688m

z[5] = 4.086m

z[6] = 4.9032m

z[7] = 5.7204m

Figure 4.8: Height profile of the Gotcha scene, using data calibrated by Algorithm 2

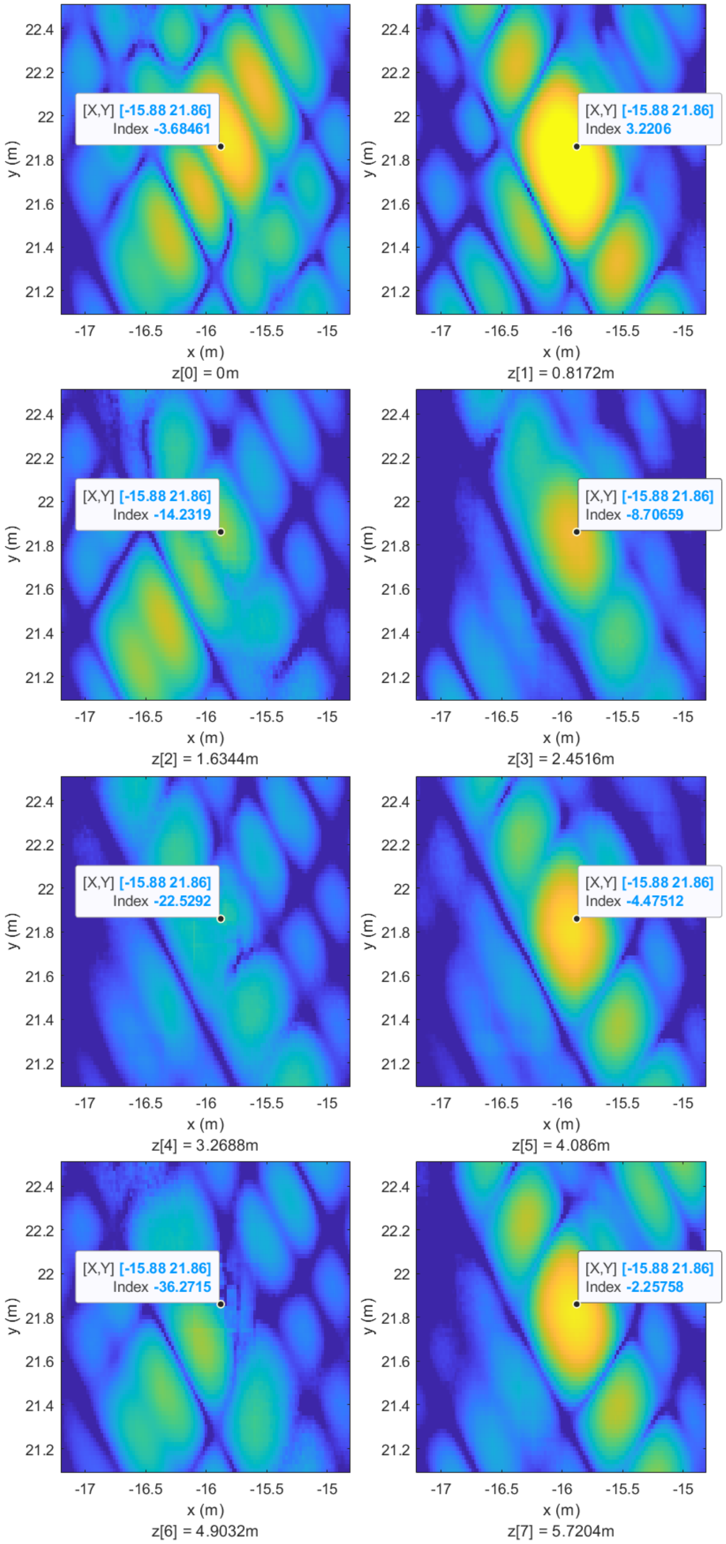

Figure 4.9: Height profile of the tophat in the Gotcha scene, using data calibrated by Algorithm 2

4.1.3 Algorithm 3

For clutter-based calibration, a subset of the scene with sufficient homogeneity of size 950 by 850 pixels is selected from each image, as shown in Figure 4.10. The autocorrelation between the homogeneous patches for successive passes is performed to determine the phase differences. The generated relative height map is shown in Figure 4.11, where very similar results to those shown in Figure 4.8 for Algorithm 2 is observed. These results also demonstrate improved sensitivity and focusing of the scatterers in elevation across the scene after calibration. As shown in Figure 4.12, a scatterer from the tophat subset of the scene similarly shows the focusing of the scatterer to $z[1]$, with a peak of 3.059 dB.

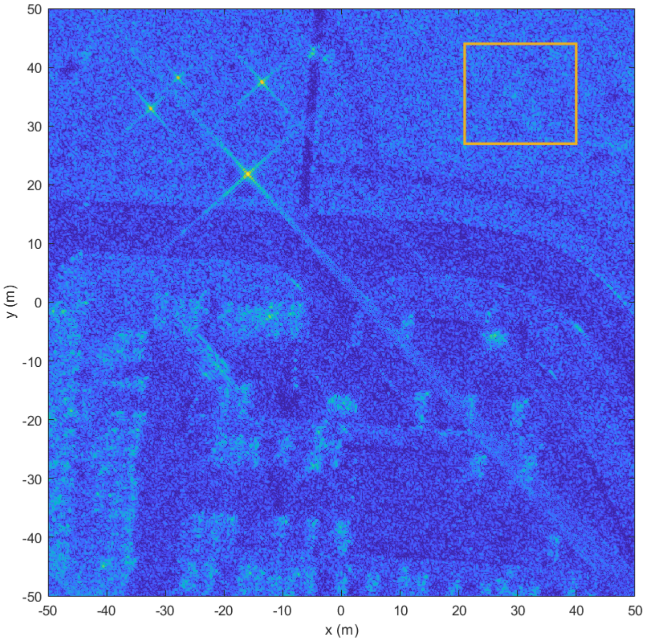

Figure 4.10: Homogeneous patch of data (orange boxed) used for clutter-based calibration

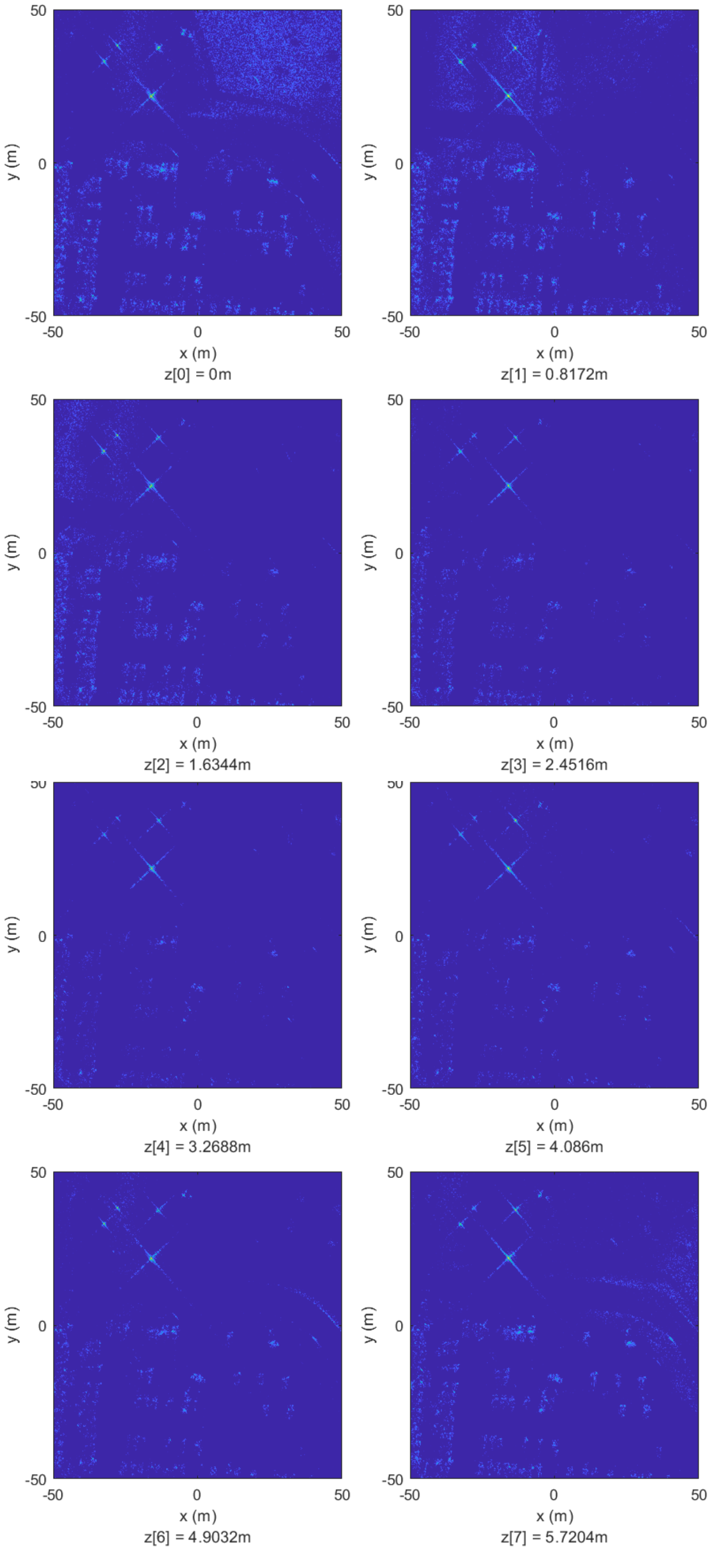

z[0] = 0m

z[1] = 0.8172m

z[2] = 1.6344m

z[3] = 2.4516m

z[4] = 3.2688m

z[5] = 4.086m

z[6] = 4.9032m

z[7] = 5.7204m

Figure 4.11: Height profile of the Gotcha scene, using data calibrated by Algorithm 3

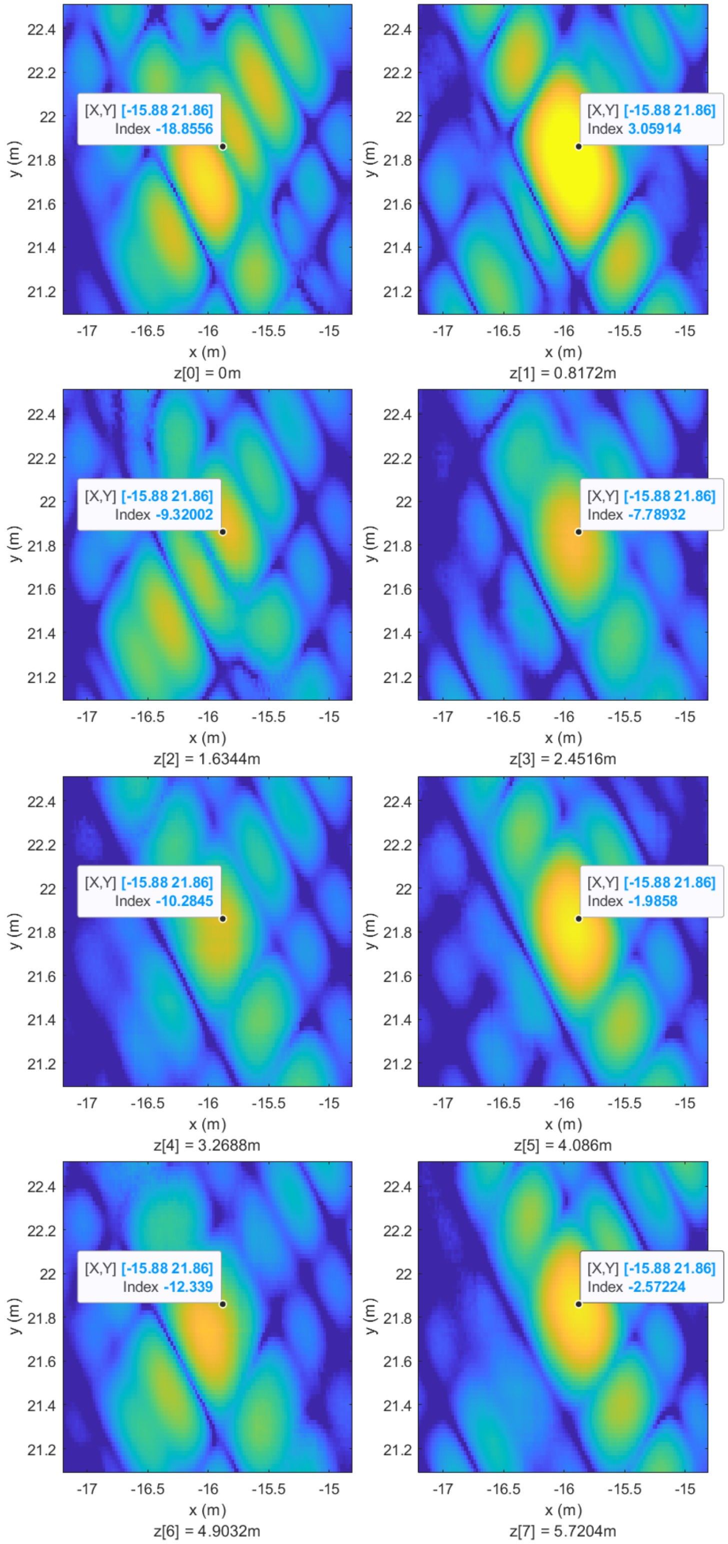

Figure 4.12: Height profile of the tophat in the Gotcha scene, using data calibrated by Algorithm 3

4.1.4 Corrected Height Map

The application of calibration algorithms 1, 2, and 3 to the IFSAR processing chain have demonstrated convergence of the scatterers in elevation in the resulting relative height maps. To continue through the processing chain and obtain the corrected height map, a point cloud consisting of the peaks of each scatterer in elevation from each relative height map is generated. A simplification of this step is performed with select areas of interest in the scene, specifically, scatterers from the top hat, calibration target (-13.86m, 37.7m), forklift, tractor, Ford Taurus, Toyota Camry, Hyundai Santa Fe, and Nissan Maxima. Table 4.1 lists the height of these objects for ground truth. The estimate of each objects' altitude is determined by where the majority of the stronger (>35 dB) peaks cluster together in the point cloud. Since the height of the tophat is known to be 1m, it is used as the reference in shifting the relative height estimates to obtain the absolute height estimates.

Table 4.1: Ground truth height of the objects of interest in the scene

Object	Height (m)
Cal Target	0.686
Tophat	1
Tractor	∼4.674
Forklift	∼2.246
Taurus	∼1.468
Camry	∼1.460
Santa Fe	∼1.676
Maxima	∼1.442

The relative and absolute estimates of the altitude of the select scatterers are summarized in Tables 4.2, 4.3, and 4.4. The results show some anomalies in the estimated heights. There is agreement in the estimated height between the calibration target and Taurus between all three algorithms. If spatial aliasing is considered, scatterers at relative height 5.72m would aliase into $z[1] = 0.817$m with a shift of 1m. With this case, the absolute height of the forklift, Santa Fe, and Maxima, also demonstrate agreement in absolute height between the algorithms. Algorithms 1 and 3 agree for the Camry, however, for Algorithm

2, it is noted that there were only a few more peaks at $z[0]$ = 0m than $z[1]$ = 0.817m in the relative height map. Algorithms 2 and 3 agree for the Tractor. Many of the scatterers in these results converged to the same height. In reality, this is not expected to be the case. For example, the tractor is expected to be at a greater height relative to the tophat. Furthermore, the scene under consideration has a slope of approximately 1.15°, as measured in Figure 4.13 [35]. This results in added height to objects and the terrain with the increase in x.

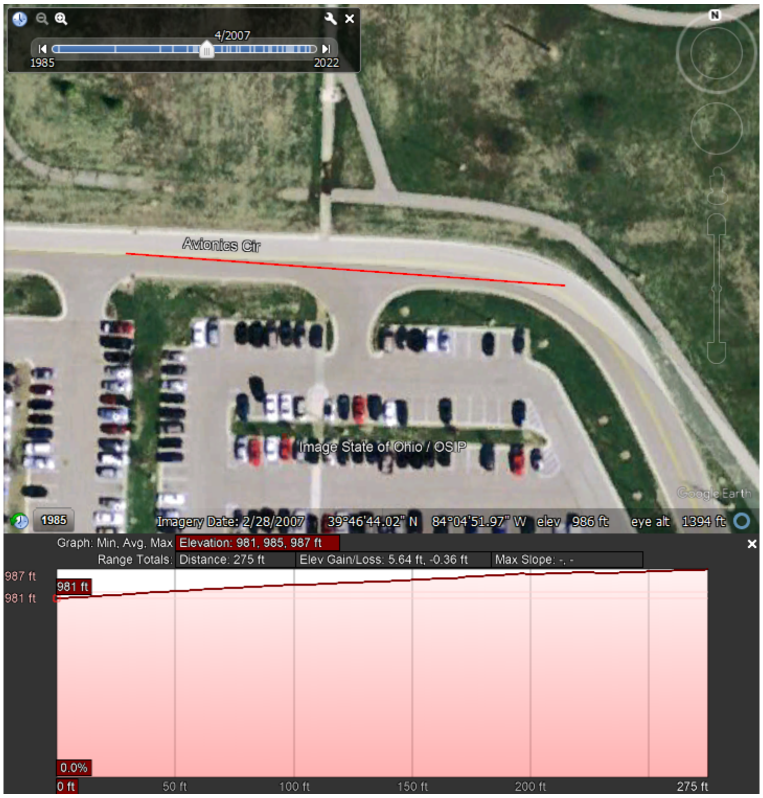

Figure 4.13: Google Earth imagery corresponding to Gotcha data, with terrain elevation measured across the scene (red path)

Table 4.2: Estimated relative and absolute altitudes for objects of interest in relative height map generated with Algorithm 1

Algorithm 1		
Object	Estimated relative z (m)	Estimated absolute z (m)
Cal Target	0	1
Tophat	0	1
Tractor	5.72	6.72
Forklift	5.72	6.72
Taurus	0	1
Camry	0	1
Santa Fe	5.72	6.72
Maxima	5.72	6.72

Table 4.3: Estimated relative and absolute altitudes for objects of interest in relative height map generated with Algorithm 2

Algorithm 2		
Object	Estimated relative z (m)	Estimated absolute z (m)
Cal Target	0.817	1
Tophat	0.817	1
Tractor	0.817	1
Forklift	0	0.183
Taurus	0.817	1
Camry	0	0.183
Santa Fe	0	0.183
Maxima	0	0.183

Table 4.4: Estimated relative and absolute altitudes for objects of interest in relative height map generated with Algorithm 3

Algorithm 3		
Object	Estimated relative z (m)	Estimated absolute z (m)
Cal Target	0.817	1
Tophat	0.817	1
Tractor	0.817	1
Forklift	0	0.183
Taurus	0.817	1
Camry	0.817	1
Santa Fe	0	0.183
Maxima	0	0.183

Several factors may have contributed to the resolved absolute height results. As is known, the resolved height of objects in the scene is dependent on the sensing geometry and phase estimates. As shown for the synthetic data, where the height of the synthetic aperture is increased, scatterers appear taller than actual. This principle may have contributed to the observed results as well as cause spatial aliasing in z. Additionally, noisy data result in high RMSE in the phases after calibration, translating to height errors. Scatterering effects may also influence the results, as reflections may not necessarily come from the top of the object. The height resolution of 0.817m may also be too coarse and objects may exist at elevations between altitude bins. All of these factors leave room for further exploration.

Chapter 5

Conclusion

Many solutions exist for addressing the sensor calibration problem. In this work, the application of 3 data-driven calibration techniques were introduced to the multi-pass IFSAR processing chain to calibrate synthetic data and generate the height map of a simulated scene. These techniques include calibration via sources of opportunity at known angles of arrival (Algorithm 1), using a contrast-based metric (Algorithm 2), and leverging the statistical properties of a homogeneous scene (Algorithm 3). The calibration algorithms were demonstrated in 2-D for a pixel in the scene, before extending it to 3-D to calibrate all of the pixels in the scene and generate the relative height map.

For the synthetic data, several scatterers at different heights were simulated and receive data were collected for 8 passes at different elevations. Phase errors were introduced to the resulting SAR images. Multi-pass IFSAR processing including a phase calibration step was then performed. With calibration, there was an evident improvement in the gain and focusing of the scatterers in the resulting height maps of Figures 3.8, 3.10, and 3.13 as compared to the height map generated using uncalibrated data in Figure 3.6. The simulated scatterers converged to their expected heights after calibration of the data with all 3 algorithms. The effect of noise on calibration performance was also explored. All algorithms performed well given low noise. Algorithm 1 showed the best overall performance while Algorithms 2 and 3 were more sensitive to noise.

The calibration algorithms were then applied the IFSAR processing of the measured Gotcha data set, where scatterers also demonstrated gain improvement and convergence in elevation in the relative height map after calibration of the SAR images. While Figures 4.5, 4.8, and 4.11 showed improvement in gain and convergence of the scatterers in altitude after calibration, suggesting some calibration success over that shown in the uncalibrated case of Figure 4.3, associating the scatterers to their absolute height and determining whether the height differences between the objects in the scene agree with the ground truth data, proved to be a challenge and additional exploration is needed.

Future work may include novel phase calibration and beamshaping algorithms as well as amplitude calibration. These techniques may be tested with different measured data sets. This work can also be extended to incorporate multiple synthetic apertures from different azimuth angles and data from different polarizations in future research.

Bibliography

[1] N. J. Kolias and M. T. Borkowski, “The development of T/R modules for radar applications,” in *2012 IEEE/MTT-S International Microwave Symposium Digest*, pp. 1–3, 2012.

[2] C. Fulton, M. Yeary, D. Thompson, J. Lake, and A. Mitchell, “Digital phased arrays: Challenges and opportunities,” *Proceedings of the IEEE*, vol. 104, no. 3, pp. 487–503, 2016.

[3] J. A. Haimerl, B. Hudson, G. P. Fonder, and D. K. Lee, “Overview of the large digital arrays of the space fence radar,” in *2016 IEEE International Symposium on Phased Array Systems and Technology (PAST)*, pp. 1–8, 2016.

[4] C. Fulton, N. Goodman, M. Yeary, R. Palmer, H. Sigmarsson, and J. McDaniel, “Preliminary system integration and performance features for an s-band, dual-polarized, all-digital phased array radar,” in *2022 IEEE/MTT-S International Microwave Symposium - IMS 2022*, pp. 862–864, 2022.

[5] U.S. Naval Research Laboratory, “NRL demonstrating advanced distributed radar concepts with FlexDAR.” https://www.nrl.navy.mil/Media/News/Article/2712331/, 2021.

[6] J. H. Huang, J. L. Garry, G. E. Smith, and D. K. Tan, “In-field calibration of passive array receiver using detected target,” in *2018 IEEE Radar Conference (RadarConf18)*, pp. 0715–0720, 2018.

[7] G. Farquharson, P. Lopez-Dekker, and S. J. Frasier, “Contrast-based phase calibration for remote sensing systems with digital beamforming antennas,” *IEEE Transactions on Geoscience and Remote Sensing*, vol. 51, no. 3, pp. 1744–1754, 2013.

[8] G. Krieger, M. Younis, N. Gebert, S. Huber, F. Bordoni, A. Patyuchenko, and A. Moreira, “Advanced digital beamforming concepts for future sar systems,” in *2010 IEEE International Geoscience and Remote Sensing Symposium*, pp. 245–248, 2010.

[9] S. Huber, M. Younis, G. Krieger, and A. Moreira, “Error analysis for digital beamforming synthetic aperture radars: A comparison of phased array and array-fed reflector systems,” *IEEE Transactions on Geoscience and Remote Sensing*, vol. 59, no. 8, pp. 6314–6322, 2021.

[10] J. P. Kroll, M. Younis, and G. Krieger, “Estimation of multi-channel sar instrument errors using a hybrid calibration system model,” in *EUSAR 2021; 13th European Conference on Synthetic Aperture Radar*, pp. 1–6, 2021.

[11] M. Younis, C. Laux, N. Al-Kahachi, P. Lopez-Dekker, G. Krieger, and A. Moreira, “Calibration of multi-channel spaceborne sar - challenges and strategies,” in *EUSAR 2014; 10th European Conference on Synthetic Aperture Radar*, pp. 1–4, 2014.

[12] J. P. Kroll, M. Younis, and G. Krieger, “Multi-channel sar instrument calibration using the spatial correlation properties of homogeneous scenes,” in *2022 23rd International Radar Symposium (IRS)*, pp. 6–9, 2022.

[13] E. Attia and B. Steinberg, “Self-cohering large antenna arrays using the spatial correlation properties of radar clutter,” *IEEE Transactions on Antennas and Propagation*, vol. 37, no. 1, pp. 30–38, 1989.

[14] S. L. Chua, “Multi-baseline interferometric synthetic aperture radar applications and error analysis,” Master’s thesis, Dept. of Electrical Engineering and Computer Science, Massachusetts Institute of Technology, Cambridge, Massachusetts, 2007.

[15] F. Baselice, A. Budillon, G. Ferraioli, V. Pascazio, and G. Schirinzi, “Multibaseline sar interferometry from complex data,” *IEEE Journal of Selected Topics in Applied Earth Observations and Remote Sensing*, vol. 7, no. 7, pp. 2911–2918, 2014.

[16] A. Reigber and A. Moreira, “First demonstration of airborne sar tomography using multibaseline l-band data,” *IEEE Transactions on Geoscience and Remote Sensing*, vol. 38, no. 5, pp. 2142–2152, 2000.

[17] S. Tebaldini and A. Monti Guarnieri, “On the role of phase stability in sar multibaseline applications,” *IEEE Transactions on Geoscience and Remote Sensing*, vol. 48, no. 7, pp. 2953–2966, 2010.

[18] M. Pardini, K. Papathanassiou, V. Bianco, and A. Iodice, “Phase calibration of multibaseline sar data based on a minimum entropy criterion,” in *2012 IEEE International Geoscience and Remote Sensing Symposium*, pp. 5198–5201, 2012.

[19] S. Tebaldini, F. Rocca, M. Mariotti d’Alessandro, and L. Ferro-Famil, “Phase calibration of airborne tomographic sar data via phase center double localization,” *IEEE Transactions on Geoscience and Remote Sensing*, vol. 54, no. 3, pp. 1775–1792, 2016.

[20] Air Force Research Laboratory, SNA, “Gotcha volumetric SAR data set, version 1.0.” https://www.sdms.afrl.af.mil/index.php?collection=gotcha, 2007.

[21] M. Longbrake, “True time-delay beamsteering for radar,” in *2012 IEEE National Aerospace and Electronics Conference (NAECON)*, pp. 246–249, 2012.

[22] R. Mailloux, *Phased Array Antenna Handbook.* Antennas and Propagation Library, Artech House, 2005.

[23] H. L. Van Trees, *Optimum Array Processing: Part IV of Detection, Estimation, and Modulation Theory*. New York, NY: John Wiley & Sons, 2002.

[24] M. Skolnik, *Introduction to Radar Systems*, 3rd ed. New York, NY: McGraw-Hill, 2001.

[25] A. W. Doerry, "Catalog of window taper functions for sidelobe control," April 2017.

[26] M. A. Richards, "A beginner's guide to interferometric sar concepts and signal processing [aess tutorial iv]," *IEEE Aerospace and Electronic Systems Magazine*, vol. 22, no. 9, pp. 5–29, 2007.

[27] A. W. Doerry, "Basics of polar-format algorithm for processing synthetic aperture radar images.," May 2012.

[28] A. W. Doerry, E. E. Bishop, and J. A. Miller, "Basics of backprojection algorithm for processing synthetic aperture radar images.," February 2016.

[29] Mathworks, "Image processing toolbox," 2022.

[30] S. N. Madsen and H. A. Zebker, "Imaging radar interferometry," in *Manual of Remote Sensing*, Jet Propulsion Laboratory, California Institute of Technology, 1994.

[31] E. Rodriguez and J. Martin, "Theory and design of interferometric synthetic aperture radars," *IEE Proceedings F (Radar and Signal Processing)*, vol. 139, pp. 147–159(12), April 1992.

[32] H. Zebker and J. Villasenor, "Decorrelation in interferometric radar echoes," *IEEE Transactions on Geoscience and Remote Sensing*, vol. 30, no. 5, pp. 950–959, 1992.

[33] F. Gatelli, A. Monti Guamieri, F. Parizzi, P. Pasquali, C. Prati, and F. Rocca, “The wavenumber shift in sar interferometry,” *IEEE Transactions on Geoscience and Remote Sensing*, vol. 32, no. 4, pp. 855–865, 1994.

[34] A. W. Doerry and D. L. Bickel, “A 3-d sar approach to ifsar processing,” March 2000.

[35] Google Earth Pro V 7.3.6.9345. (February 28, 2007). Wright Patterson AFB, Ohio. 39° 46’ 44.02” N, 84° 04’ 51.97” W, Eye alt 1394 ft. State of Ohio/OSIP.